



Molecular viscosity and diffusivity effects in transitional and shock-driven mixing flows

F. S. Pereira *, F. F. Grinstein, D. M. Israel, and R. Rauenzahn
 Los Alamos National Laboratory, Los Alamos, New Mexico 87545, USA

 (Received 21 August 2020; revised 10 December 2020; accepted 17 December 2020; published 19 January 2021)

This paper investigates the importance of molecular viscosity and diffusivity for the prediction of transitional and shock-driven mixing flows featuring high and low Reynolds and Mach number regions. Two representative problems are computed with implicit large-eddy simulations using the inviscid Euler equations (EE) and viscous Navier-Stokes equations (NSE): the Taylor-Green vortex at Reynolds number $Re = 3000$ and initial Mach number $Ma = 0.28$, and an air-SF₆-air gas curtain subjected to two shock waves at $Ma = 1.2$. The primary focus is on differences between NSE and EE predictions due to viscous effects. The outcome of the paper illustrates the advantages of utilizing NSE. In contrast to the EE, where the effective viscosity decreases upon grid refinement, NSE predictions can be assessed for simulations of flows with transition to turbulence at prescribed constant Re . The NSE can achieve better agreement between solutions and reference data, and the results converge upon grid refinement. On the other hand, the EE predictions do not converge with grid refinement, and can only exhibit similarities with the NSE results at coarse grid resolutions. We also investigate the effect of viscous effects on the dynamics of the coherent and turbulent fields, as well as on the mechanisms contributing to the production and diffusion of vorticity. The results show that nominally inviscid calculations can exhibit significantly varying flow dynamics driven by changing effective resolution-dependent Reynolds number, and highlight the role of viscous processes affecting the vorticity field. These tendencies become more pronounced upon grid refinement. The discussion of the results concludes with the assessment of the computational cost of inviscid and viscous computations.

DOI: [10.1103/PhysRevE.103.013106](https://doi.org/10.1103/PhysRevE.103.013106)

I. INTRODUCTION

The Navier-Stokes equations (NSE) are a set of partial differential equations used to describe the macroscopic motion of continuous fluid media. For problems involving variable-density flow due to multimaterial and compressibility effects, this mathematical model is defined by the conservation equations for mass, momentum, total energy, and fluid species [1,2]:

$$\frac{\partial \rho}{\partial t} + \frac{\partial(\rho V_i)}{\partial x_i} = 0, \quad (1)$$

$$\frac{\partial(\rho V_i)}{\partial t} + \frac{\partial(\rho V_i V_j)}{\partial x_j} = -\frac{\partial P}{\partial x_i} + \frac{\partial \sigma_{ij}}{\partial x_j}, \quad (2)$$

$$\frac{\partial(\rho E)}{\partial t} + \frac{\partial(\rho E V_j)}{\partial x_j} = \frac{\partial}{\partial x_j} (-P V_j + \sigma_{ij} V_i - q_j^c - q_j^d), \quad (3)$$

$$\frac{\partial(\rho c_n)}{\partial t} + \frac{\partial(\rho c_n V_j)}{\partial x_j} = -\frac{\partial J_j^n}{\partial x_j}, \quad (4)$$

where t is the time, x_i are the coordinates of a Cartesian coordinate system, ρ is the fluids' density, V_i are the Cartesian velocity components, P is the pressure, and σ_{ij} is the viscous-stress tensor which for Newtonian fluid equals

$$\sigma_{ij} = \mu \left(\frac{\partial V_i}{\partial x_j} + \frac{\partial V_j}{\partial x_i} - \frac{2}{3} \frac{\partial V_k}{\partial x_k} \delta_{ij} \right). \quad (5)$$

Furthermore, μ is the fluid's dynamic viscosity, δ_{ij} is the Dirac delta function, $E = \frac{1}{2} V_i^2 + e$ is the total energy, e is the internal energy, q^c is the conductive heat flux, q^d is the interdiffusional enthalpy flux, c_n is the mass concentration of material n , and J^n is the mass fraction diffusivity of material n . This system of equations requires constitutive relations to close. Here, we use the perfect gas relation,

$$P = (\gamma - 1)\rho e, \quad (6)$$

Fourier's law of thermal conduction,

$$q_j^c = -\kappa \frac{\partial T}{\partial x_j}, \quad (7)$$

Cook's [2] model for the interdiffusional enthalpy flux,

$$q_j^d = \sum_{n=1}^{n_t} h_n J_j^n, \quad (8)$$

and Fick's law of diffusion,

$$J_j^n = \rho \mathcal{D} \frac{\partial c_n}{\partial x_j}. \quad (9)$$

In these closure models, γ is the specific heat ratio, T is the temperature, h_n is the enthalpy of a material n , n_t is the number of materials, and κ and \mathcal{D} are the thermal conductivity and diffusivity coefficients.

For high Reynolds number turbulent flow, it is not feasible to perform a true direct-numerical simulation (DNS), which fully resolves all the scales of motion that the NSE give rise

*fspereira@lanl.gov

to. It is therefore necessary to model either some or all the turbulent scales: just the smaller scales in large-eddy simulation (LES), or all turbulent scales in Reynolds-averaged Navier-Stokes (RANS) simulation. In this case, the quantities in the NSE are re-interpreted as averaged quantities, and additional model terms may be added to the equations to model the unclosed terms that appear due to the averaging procedure.

Although there are many explicit turbulence models which can be employed, this paper primarily considers the implicit LES (ILES) method. An ILES is defined as a simulation which uses the original NSE, along with a numerical solution procedure with certain specific properties [3] such that numerical diffusion of the scheme behaves like a turbulence model. Thus, in ILES, an implicitly provided numerical sub-grid model captures the physical effects of the unresolved scales of the turbulence. This is in contrast to a DNS, in which turbulent scales of motion are fully resolved down to the Kolmogorov dissipation length scale. Note that, since not all numerical schemes have the correct truncation properties, we can say that while all ILES simulations can be viewed as under-resolved DNS, not all under-resolved DNS is ILES.

In cases involving high Mach, Ma , and Re numbers (e.g., stellar astrophysics [4–6], shock-driven turbulent mixing [7–9], detonation [10–12], and high-speed combustion [13–15]), the Navier-Stokes equations are often simplified to their inviscid form. This simplification is typically justified by arguing that the magnitudes of the molecular diffusion terms are expected to be small compared to the corresponding turbulent transport terms, which, in the case of ILES, are represented by the numerical diffusion. This implies that σ_{ij} , q^c , q^d , and J^n can be neglected. The resulting set of governing equations are the inviscid Euler equations (EE). Another justification for ignoring the molecular diffusion terms is the assumption that a flow at sufficiently high Re becomes Reynolds number independent, and converges to the infinite Reynolds number solution.

A consequence of assuming inviscid flow is that the system of Eqs. (1)–(4) changes from second-order parabolic to first-order hyperbolic [16–20]. Along with the smaller number of terms, this mathematical property reduces the cost of solving the EE owing to the availability of highly tested and efficient numerical algorithms [16–20]. This is one reason the EE approach is so common.

However, despite its ubiquity, there is little formal analysis and few numerical studies to justify the use of the EE, or identify its range of validity. In fact, there are several reasons to question its widespread use. This is what the current paper is intended to investigate.

The practical envelope of the EE framework is typically not precisely defined, i.e., for what ranges of Re , Ma , flow conditions, and grid resolutions is the assumption of inviscid fluid acceptable? Previous studies by one of the authors [21–24] demonstrate (i) the importance of (turbulent) viscosity in ship hydrodynamic simulations even at $Re = 2.03 \times 10^9$; (ii) the relevance of Re in transitional flows; and (iii) the reduced flow Ma that shock-driven turbulent mixing problems can achieve. These studies motivate further assessments of EE based simulations in transitional flows driven by hydrodynamic instabilities.

In addition, there are other reasons to be skeptical of using the EE. First, although the global Re may be high, flows which include transition will include regions where viscous effects will be important, and these effects may change the subsequent flow evolution. Second, there remains the question of how high a Re is high enough. A true separation between the large structures and the dissipation scales may require a decade or decades of inertial range, which may not exist except for geophysical and astrophysical turbulence where $Re \sim \mathcal{O}(10^{10})$ or higher [25]. Studies show that for EE ILES, there is a flattening of the turbulent energy spectrum that starts near the dissipation scale, and extends to significantly larger scales. This effect is not present in the (lower Re) NSE simulations [26]. Finally, neglecting viscosity can only be correct for certain quantities of interest. For example, while turbulent kinetic energy, which is dominated by the large scale structures, should match data for reasonable grids, enstrophy, which is dominated by the small scales, will actually diverge with refinement.

Transition to turbulence can lead to an inertial range exhibiting Kolmogorov's $-5/3$ wave-number power law in the turbulence kinetic energy spectrum for sufficiently high Re [27,28] above the mixing transition threshold, $Re \sim 1-2 \times 10^4$ based on the integral length scale L (or $Re \sim 1-1.4 \times 10^2$ based on the Taylor microscale) [27]. A higher threshold, $Re \sim 1.6 \times 10^5$, is needed to achieve a minimum turbulent state [28]—proposed as having enough large or small scale separation to ensure robustness of macroscopic flow characteristics. Transition is inherently initial conditions dependent—e.g., [29–31]. Viscous effects are thus expected to matter less for sufficiently high Reynolds numbers, Re .

The idea that viscosity effects would be important only at very short scales in shock-tube problems of interest was suggested in early work by Mikaelian [32]. On the other hand, plasma viscosity effects growing with temperature as $\approx T^{2.5}$ become important in inertial confinement fusion hot spots ($T \sim \text{keV}$). For example, this is demonstrated in the studies of turbulence inhibition by viscous dissipation by Weber *et al.* [33], where Re at the gas hot spot was found to be $Re \sim 10-100$, quite far from the $Re \sim 10\,000$ transition threshold. Addressing the detailed impact of viscous effects in applications at scale becomes particularly important as recent advances in computer science and resources promise to provide significant reductions in numerical diffusion, and it becomes feasible to accurately capture these effects in the future simulations.

From a verification and validation perspective, the application of the EE also raises concerns since it hampers the quantification of numerical and modeling errors. This results from the fact that the effective flow Re , Re_e , of the simulations is not bounded. We define effective Reynolds number as

$$Re_e \equiv \frac{V_0 L_0}{\nu_e}, \quad (10)$$

where L_0 and V_0 are a reference length scale and velocity, and ν_e is the effective viscosity,

$$\nu_e = \nu + \nu_n + \nu_t, \quad (11)$$

which is composed of the physical ν , numerical ν_n , and turbulent (closure model) ν_t viscosities. Since $\nu = 0$ for in-

viscid flow and $\nu_t = 0$ (ideally) for laminar flow, the effective Reynolds number is determined by the numerical viscosity in EE computations. However, ν_n reduces upon spatiotemporal grid refinement which makes Re_e increase. Finally, it is important to emphasize that the utilization of numerical diffusion to model the terms involving \mathcal{D} and ν also affects the remaining inviscid terms of the EE [Eqs. (1)–(4): $\rho V_i, \rho V_i V_j, P, PV_j, \dots$].

This paper analyzes the importance of molecular viscosity and diffusivity effects on the prediction of transitional and shock-driven turbulent mixing flows featuring high and low Re and Ma regions. For high Re , the flow mostly features high-intensity or fully developed turbulence, and so (Re dependent) phenomena like the onset of turbulence may play a minor role in the flow dynamics. However, there are many flows of practical interest featuring regions of low and high Re , where viscous dependencies of the onset of turbulence are essential and must be captured. In the (low Re) transient and transitional regions, where the separation of scales may be questionable and spectra are narrow, the physical or/and numerical viscosity play an important point in the flow physics. Furthermore, the history of the transition process may persist, so capturing the viscous effects may be essential to matching the overall history of the flow. Our main focus is on assessing viscous effects; assessing molecular diffusivity effects on scalar predictions deserves further study which is not part of the current scope.

Two representative flows are calculated with ILES [3,34] using the EE and NSE: (i) the Taylor-Green vortex (TGV) [35] at $Re = 3000$ [36] and initial $Ma = 0.28$; and (ii) the air-SF₆-air varicose gas curtain subjected to two shock waves at $Ma = 1.2$ studied by Balakumar *et al.* [37]. The first case assesses the effect of viscous phenomena in single-fluid transitional flow, whereas the second also includes material mixing, diffusivity, high and low flow Ma regions, and shock waves. The simulations are conducted for different grid resolutions to assess the effects of numerical diffusion on the flow dynamics, quantities of interest, and inviscid flow assumption. The predictions are compared against reference data [36–38], and their computational cost analyzed. The paper also evaluates the effect of the molecular viscosity and diffusivity on the turbulence and coherent fields, as well as on the mechanisms contributing to the production of vorticity.

The remainder of the paper is structured as follows. The test cases and simulations are described in Sec. II. This includes details about the reference experiments, numerical settings, and solver [39]. The results are then discussed in Sec. III, and the conclusions are summarized in Sec. IV.

II. FLOW PROBLEMS AND NUMERICAL DETAILS

A. Taylor-Green vortex

The TGV [35] is an archetypal flow problem for modeling and simulation of turbulence onset, development, and decay. This flow is initially characterized by multiple laminar vortices as illustrated in Fig. 1(a). These coherent structures evolve and interact in time, and eventually lead to turbulent flow by the action of vortex stretching and reconnection without need for background perturbations [36,40,41].

Since viscous processes are expected to have a role in the onset of the reconnection phenomenon [40], there has been in-

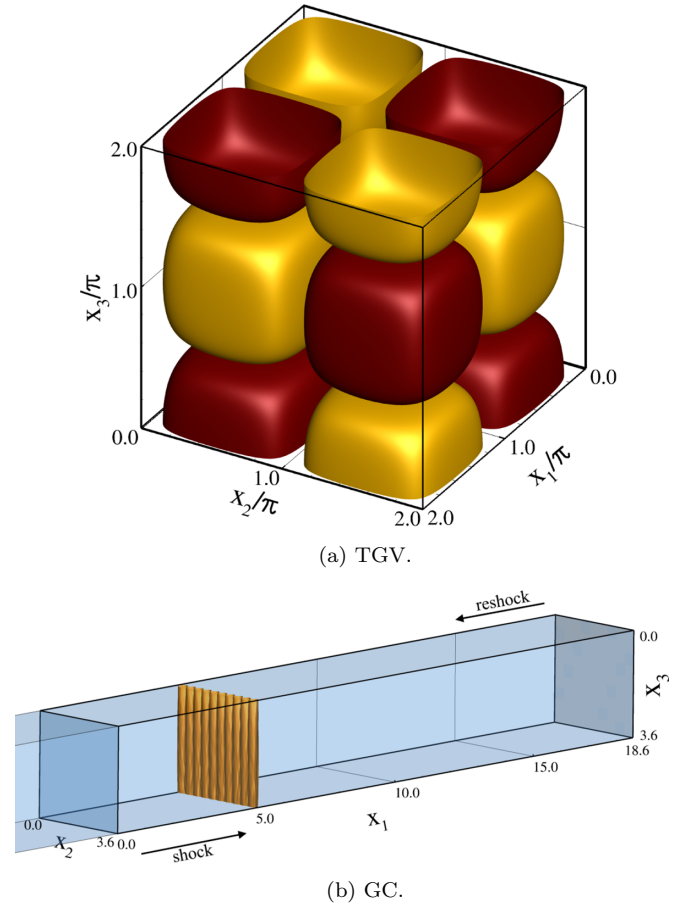


FIG. 1. Initial flow fields of the selected test cases.

tense debate about the potential existence of flow singularities in inviscid EE calculations [36,42–47]. Nevertheless, the basic (convectively driven) physics of reconnection [48,49] and turbulence decay [50] can be captured with a well-designed EE based ILES having adequate nonvanishing residual numerical diffusion (recent survey in [51]). The flow kinetic energy is expected to decay (e.g., [52]) after the development of turbulence. The TGV case has been also used to demonstrate how the convective numerical diffusion of certain algorithms can be used to emulate the dominant subgrid scale physics of transition to turbulence and decay for high (but finite) Re flows [38,53] in ILES.

The numerical simulations of the TGV are conducted in a cubical computational domain defined in the Cartesian coordinate system (x_1, x_2, x_3) shown in Fig. 1(a). The length of the domain is $L/L_0 = 2\pi$ (L_0 is a reference length scale), and periodic boundary conditions are prescribed at all faces. The initial velocity and pressure fields [35] are

$$V_1(\mathbf{x}) = V_o \sin(x_1) \cos(x_2) \cos(x_3), \quad (12)$$

$$V_2(\mathbf{x}) = -V_o \cos(x_1) \sin(x_2) \cos(x_3), \quad (13)$$

$$V_3(\mathbf{x}) = 0, \quad (14)$$

$$P(\mathbf{x}) = P_o + \frac{\rho_o V_o^2}{16} [2 + \cos(2x_3)][\cos(2x_1) + \cos(2x_2)], \quad (15)$$

where V_o , P_o , and ρ_o stand for the velocity, pressure, and density magnitudes at the initial time instant, $t = 0$. The calculations are conducted with a compressible flow solver [39] using the ideal gas equation of state. This option leads to maximum instantaneous and averaged (L_1 norm) variations of ρ that can reach 11.0 and 1.4% of ρ_o , respectively. In viscous calculations, the $Re = \rho_o L_o V_o / \mu$ is set equal to 3000 to match the DNS studies of Brachet *et al.* [36] and Drikakis *et al.* [38]. The initial thermodynamic and flow properties are the following: $Ma_o = 0.28$, $V_o = 10^4$ cm/s, $L_o = 1.00$ cm, $\rho_o = 1.178 \times 10^{-3}$ g/cm³, $P_o = 10^5$ Pa, $\mu = 3.927 \times 10^{-3}$ g/(cm s), and heat capacity ratio $\gamma = 1.40$.

B. Shocked gas curtain

The gas curtain flow of Balakumar *et al.* [37] has been designed to investigate the physics of shock-driven turbulent mixing and provide validation data for numerical simulations. This classical transitional mixing problem initialized with an air-SF₆-air gas curtain contained inside a horizontal shock tube with a square cross section of 76.2 mm. The curtain is located at 137 mm from the tube's end wall and composed of a mixture of air, SF₆, and acetone to enable the use of planar laser-induced fluorescence technique to measure the density field. This experimental technique reduces the Atwood number of the gas curtain in comparison to the pure air-SF₆ case ($At = 0.67$) [54]. The curtain is generated by an array of 21 jets of 3-mm diameter and separated by 3.6 mm. The shock wave is created by the rupture of a diaphragm separating the driven and driver gases, air and nitrogen. These fluids are initially at rest and at pressures of 103 421 and 75 000 Pa, respectively.

The present problem starts with the rupture of the membrane separating the former gases. This generates a shock wave that travels along the shock tube and strikes the gas curtain at $t = 0$. At this instant, momentum is transferred to the perturbed air-SF₆ interface, which leads to its acceleration and initiates the mixing of the two fluids by baroclinic production of vorticity. Afterward, the Richtmyer-Meshkov instability and coherent structures [55,56] start developing. This step may lead to secondary hydrodynamics instabilities such as the Rayleigh-Taylor [57,58] and Kelvin-Helmholtz [59,60] instabilities. The shock wave reflects off of the end wall of the experimental facility and causes a reshock at $t = 600$ μ s (the instant when the reflected shock wave passes the gas curtain). This phenomenon triggers transition to turbulence, which enhances the mixing rate of the two materials. Brouillette [61] and Zhou [62,63] provide comprehensive descriptions of this class of flows.

The numerical simulations are conducted in a rectangular computational domain defined in the Cartesian coordinate system (x_1, x_2, x_3) shown in Fig. 1(b). The origin is located at the intersection of the plane defining the position of the initial shock wave and the left and top boundaries of the shock tube, with the x_1 axis aligned with the shockwise direction, x_2 with the transverse direction, and x_3 with the vertical direction. The gas curtain is initially at 138 mm from the end wall, and the cross section of the shock tube includes ten out of the 21 jets used in the experiments, so the computational domain is 36 mm wide. The initial

flow conditions of the gas curtain are extracted from the DNS results of Gowardhan and Grinstein [54]. Reflective conditions are prescribed at the x_1 and x_3 boundaries, whereas periodic conditions are set at $x_2 = 0$ and 36 mm. The left boundary is at $x_1 = -400$ mm so that the reflected shock wave does not reach it during the simulation time of 1200 μ s. The shock wave is initially at $x_1 = 0$ and time is given with reference to the moment the shock wave strikes the upstream interface of the gas curtain ($t = 0$). Reshock (R) is completed at $t = 600$ μ s. The fluid and thermodynamic properties of SF₆, compressed air (air₁), and ambient air (air₂) are $\gamma_{\text{air}_1} = \gamma_{\text{air}_2} = 1.40$, $\gamma_{\text{SF}_6} = 1.09$, $\rho_{\text{air}_1} = 1.28 \times 10^{-3}$ g/cm³, $\rho_{\text{air}_2} = 0.95 \times 10^{-3}$ g/cm³, $\rho_{\text{SF}_6} = 4.85 \times 10^{-3}$ g/cm³, $\mu_{\text{air}_1} = \mu_{\text{air}_2} = 1.80 \times 10^{-4}$ g/(cm s), $\mu_{\text{SF}_6} = 1.50 \times 10^{-4}$ g/(cm s), $\mathcal{D} = 9.22 \times 10^{-2}$ cm²/s. Since μ and \mathcal{D} were not measured by Balakumar *et al.* [37], the values of these quantities are extrapolated from Charonko and Prestridge [64] and tables available in literature [65]. We also assume γ , μ , and \mathcal{D} independent of the air's pressure. The complete description of the numerical setup and case is given in Pereira *et al.* [24].

C. Numerical settings

All calculations are conducted with the flow solver XRAGE [39]. This code utilizes a finite volume approach to solve the compressible and multimaterial conservation equations for mass, momentum, energy, and species concentration. The resulting system of governing equations is resolved through the Harten-Lax-van Leer-Contact [66] Riemann solver using a directionally unsplit strategy, direct remap, parabolic reconstruction [67], and the low Mach number correction proposed by Thornber *et al.* [68]. The equations are discretized with second-order accurate methods: the spatial discretization is based on a Godunov scheme, whereas the temporal discretization relies on the explicit Runge-Kutta scheme known as Heun's method. The time step, Δt , is defined by imposing a maximum CFL number equal to 0.45. Thus,

$$\Delta t = \frac{\Delta x \times \text{CFL}}{N(|V| + c)}, \quad (16)$$

where c is the speed of sound, and N is the number of spatial dimensions. The code can utilize an adaptive mesh refinement (AMR) algorithm for following waves, especially shock waves and contact discontinuities. This option is only used for the gas curtain flow. The modeling of miscible material interfaces and high convection-driven flows is performed with a van-Leer limiter [69], without artificial viscosity, and with no material interface treatments [53,70]. XRAGE uses the assumption that cells containing more than one material are in pressure and temperature equilibrium as a mixed cell closure. For the present paper, we modified the XRAGE plasma module [71–73] in order to consider the kinematic viscosity (ν) and diffusivity (\mathcal{D}) terms of the multimaterial NSE. In these cases, the effective physical viscosity is defined as

$$\nu = \sum_{n=1}^{n_t} \nu_n f_n, \quad (17)$$

where n is the material index, n_t is the number of materials, and f_n is the volume fraction of material n . The thermal flux,

q^c , in Eq. (3) is neglected in this paper. Although this should not affect the TGV case, this term would be necessary for a careful validation comparing to the experimental gas curtain data [2,74]. However, for this paper including only the dominant diffusion terms should be sufficient to observe the trends we wish to investigate. Also, evaluation of the temperature field of the gas curtain flow has shown that the instantaneous difference between its minimum and maximum value in the entire domain does not exceed 15.1%. The exception occurs during the instants of reshock where the differences can reach 42%. Considering that the temperature differences between neighboring cells are significantly smaller, these results suggest that including the heat flux would not alter the conclusions of the paper.

The selected spatial grid resolution and simulation time of the calculations are problem dependent. Whereas the TGV flow is computed for 20 time units on uniform Cartesian grids with 128^3 , 256^3 , 512^3 , and 1024^3 cells, the gas curtain calculations rely on an AMR algorithm to optimize the use of computational resources. We use three grids g_i with the same baseline grid resolution $\Delta = 2$ mm but with a different number of refinement levels. These are 4 for g_1 , 5 for g_2 , and 6 for g_3 and lead to a minimum cell size ranging from 0.25 to 0.06 mm. The selected refinement criterion is based on the magnitude of the pressure and density gradients [39]. Figure 2 illustrates the evolution of the number of cells, N_c , on the three grids for EE and NSE simulations. It shows that the finest grid resolution can reach 480.8×10^6 cells and, most notably, that the NSE simulations require fewer cells than the EE. In contrast, Table I indicates that the NSE simulations lead to smaller time steps than the EE. These differences are discussed in Sec. III B.

III. RESULTS AND DISCUSSION

The effect of molecular viscosity and diffusivity on the selected test cases is now investigated. Each problem is studied individually, and the quantities of interest comprise mean-flow, coherent, and turbulence variables. The analysis of the simulations includes the evaluation of the mechanisms contributing to the production of vorticity. The discussion concludes with the computational cost of the calculations.

A. Taylor-Green vortex

The TGV flow is initially defined by the set of laminar vortices shown in Fig. 1(a). These coherent structures interact and evolve in time, leading to the onset of turbulence. Since the TGV is an isolated system (no energy sources), the total kinetic energy of the problem decays in time due to viscous [ν_e , Eq. (11)] effects.

The temporal evolution of the mean total kinetic energy,

$$k = \frac{1}{2V_o^2} \frac{\overline{\rho v_i v_i}}{\bar{\rho}}, \quad (18)$$

predicted with the EE and NSE is depicted in Fig. 3. In Eq. (18), k is Favre averaged [75–78], the bar operator denotes a spatially averaged quantity $\bar{\Phi}$, and we adopt Einstein's summation convention.

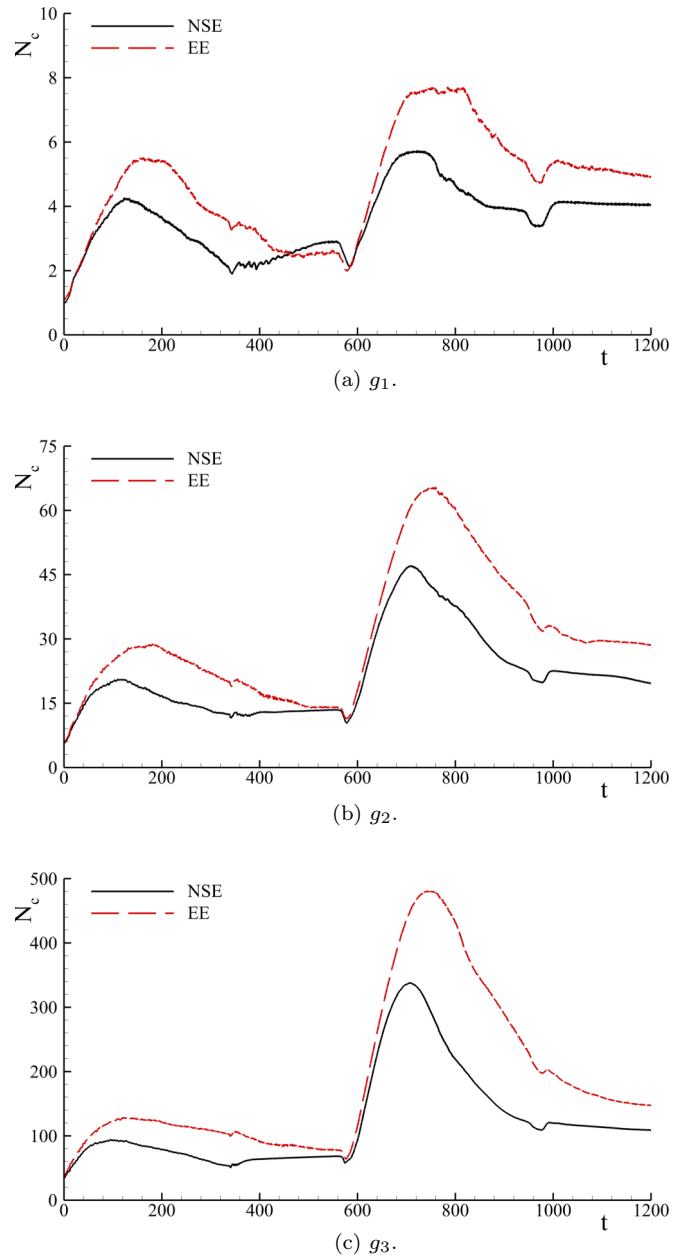


FIG. 2. Temporal evolution of the number of grid cells ($N_c \times 10^{-6}$) of gas curtain simulations for EE and NSE on different grids g_i .

Figures 3(a) and 3(c) show the temporal evolution of k for computations utilizing the EE and various spatiotemporal grid resolutions. Similar to Shu *et al.* [79], it is observed that the magnitude of k remains nearly constant during the first time instants. Yet, the length of this period, Δt , depends on the grid resolution. Whereas $\Delta t \approx 4$ for the coarsest grid, this period exceeds five time units for the finest resolution. The origin of this difference lies in the reduction of numerical diffusion caused by grid refinement. This delays the decay of k due to the smaller values of ν_e [Eq. (11)] which, in turn, increase Re_e [Eq. (10)]. Nevertheless, the most significant result in these figures is the small growth of k during this initial period. Although smaller than 0.4% of k_o , recall that the TGV

TABLE I. Minimum and maximum time step, Δt , of gas curtain simulations with EE and NSE on different grids g_i .

Grid	Model	$(\Delta t)_{\min}$	$(\Delta t)_{\max}$
g_1	NSE	8.00×10^{-9}	8.00×10^{-8}
	EE	1.38×10^{-8}	1.39×10^{-7}
g_2	NSE	4.00×10^{-9}	4.00×10^{-8}
	EE	6.90×10^{-9}	7.00×10^{-8}
g_3	NSE	2.00×10^{-9}	2.03×10^{-8}
	EE	3.50×10^{-9}	3.50×10^{-8}

represents an isolated system, and the total energy is conserved by the governing equations of the mathematical model. Thus, the observed growth in k can only occur by the conversion of internal into kinetic energy, so that $k > k_o$. Although not clearly visible in Fig. 3(a), this behavior becomes more pronounced upon grid refinement. It is also interesting to note that Morf *et al.* [80] and Brachet *et al.* [36] estimated the possibility of the occurrence of a flow singularity between 4.2 and 5.2 time units for inviscid calculations. After this initial laminar flow period, $t \approx 4-5$, the kinetic energy starts dissipating, and the flow becomes turbulent. The results also indicate that for the EE the decay rate of k depends on the grid resolution.

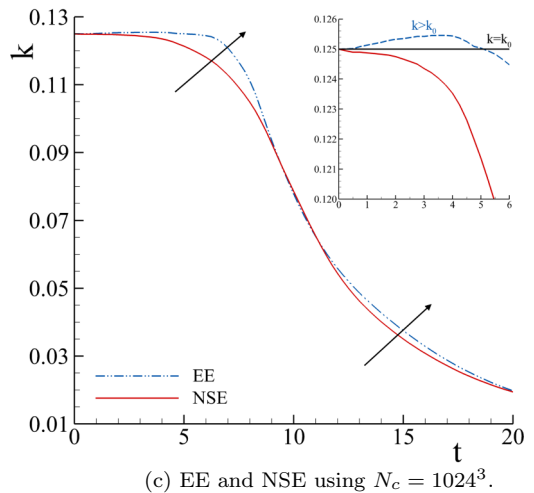
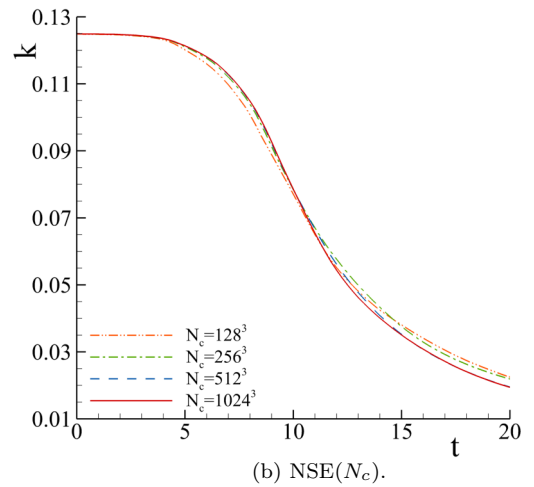
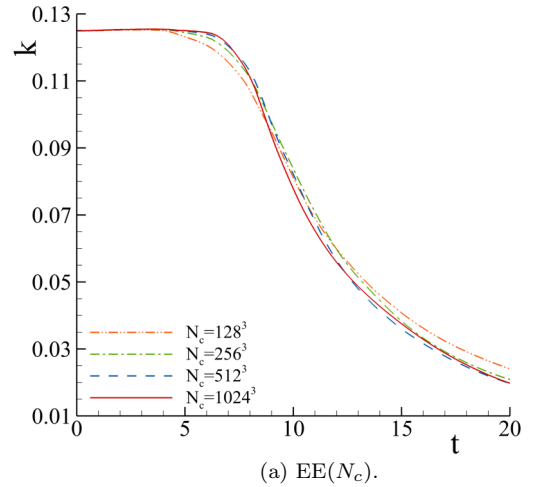
The NSE results depicted in Figs. 3(b) and 3(c) exhibit distinct tendencies. First, the decay of kinetic energy begins immediately after $t = 0$ so that $k(t)$ never exceeds k_o . Second, the solutions of the three finest grids are nearly identical until $t \approx 11$. After this instant, it is possible to identify small discrepancies that are caused by the grid resolution. This is quantified in Fig. 4 through the numerical uncertainty (gray area) [81], $U_n(k)$, of the simulations on $N_c = 512^3$ and 1024^3 . Here, $U_n(k)$ is computed with the method of Eça and Hoekstra [82] which uses an estimated uncertainty interval containing the exact solution of the mathematical model with 95% confidence, instead of an exact error, which would require knowing the true solution exactly. A detailed description of the method and the concept of numerical uncertainty is given in [81,82]. The results show that $U_n(k)$ is negligible until $t \approx 11$, but starts growing after this instant. This is caused by the development of turbulence and leads to values of $U_n(k)$ that can reach 24.2% on $N_c = 512^3$, and 8.4% on $N_c = 1024^3$. These values of $U_n(k)$ indicate that $N_c = 1024^3$ is adequate for the present paper, and that DNS studies using similar numerical settings would require finer grids to achieve U_n close to zero for k and higher-order moments.

Next, Fig. 5 presents the temporal evolution of the averaged total kinetic energy dissipation, ε :

$$\varepsilon = -\frac{\partial k}{\partial t}. \quad (19)$$

The predictions are compared against the simulations of Brachet *et al.* [36] (incompressible) and Drikakis *et al.* [38] (compressible) at $Re = 3000$. Focusing on the EE predictions plotted in Fig. 5(a), these exhibit a close dependence on the grid resolution, and evidence the existence of five distinct periods where the simulations are in poor agreement with the reference data [36,38].

(i) Until $t \approx 3-4$, the predicted dissipation [Eq. (19)] is negative, which indicates that k is being generated. This is


 FIG. 3. Temporal evolution of kinetic energy, k , for EE and NSE on different grid resolutions.

in agreement with the EE results of Fig. 3 and stems from the aforementioned conversion of internal into kinetic energy.

(ii) After this initial period, the kinetic energy of the flow starts being dissipated. Yet, the absence of physical viscosity and the successive grid refinement make the EE underpredict the magnitude of ε until $t = 6$. Considering $t = 5$, the dissi-

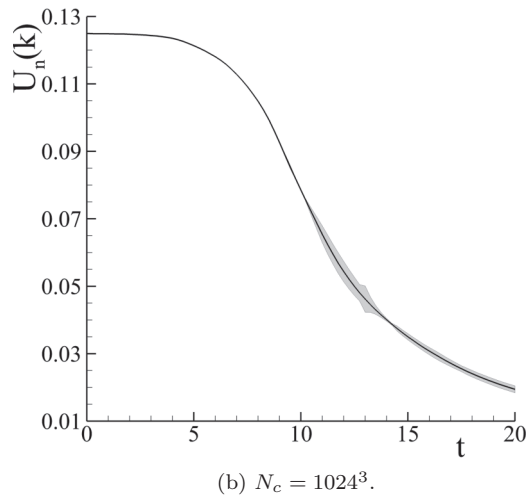
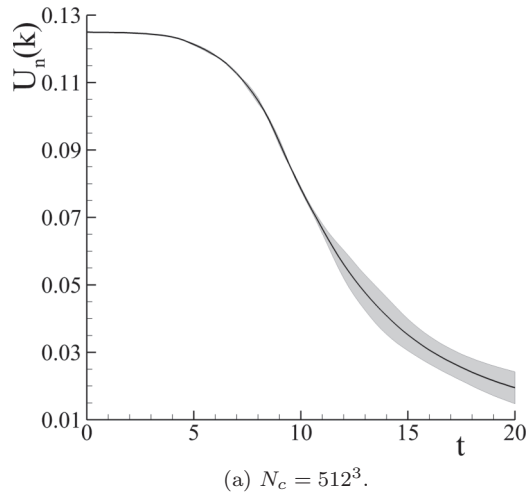


FIG. 4. Temporal evolution of kinetic energy, k , and respective numerical uncertainty, $U_n(k)$, for EE and NSE on grids with $N_c = 512^3$ and 1024^3 .

pation predicted by DNS [36] is equal to 2.6×10^{-3} , whereas for the EE it does not exceed 0.3×10^{-3} . We emphasize that the onset of turbulence occurs during this period [36]. As the flow undergoes transition, energy cascades to smaller scales at which dissipation occurs. Since for the EE the dissipation is purely numerical, and happens primarily at the smallest resolved scales, the growth of ε is delayed until a sufficient cascade can develop.

(iii) Afterward, ε starts growing at a much faster rate than observed in the reference studies and NSE. This stems from the rapid development of increased fine scale motions, as shown in Fig. 6 for the EE, which is due to the cascade of energy that would have otherwise been dissipated by molecular viscosity at coarser scales in the NSE. Also, the solutions of ε do not converge upon grid refinement, since in the true infinite Reynolds number limit, the inertial range would extend to infinite wave number and the enstrophy spectrum would not converge.

(iv) The magnitude of ε starts diminishing in time. Yet, it is possible to identify a second peak of ε for the three coarsest grids. Since this peak is not observed on the finest grid nor

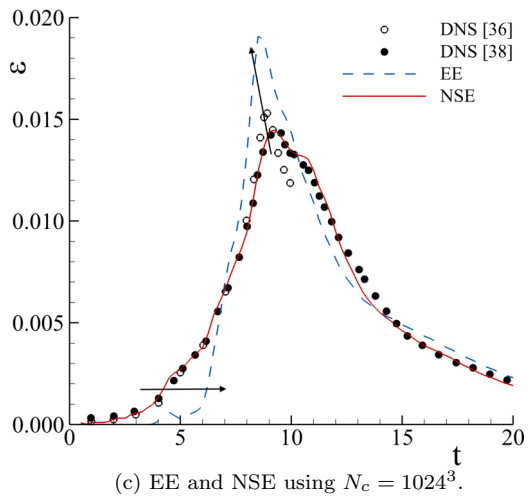
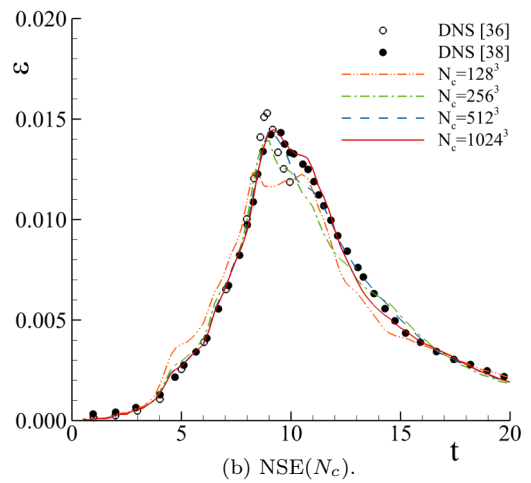
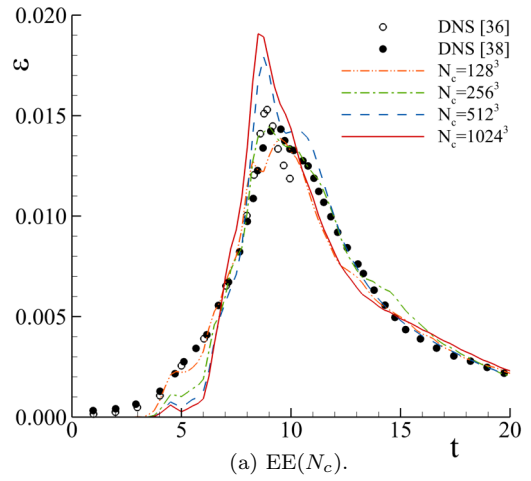
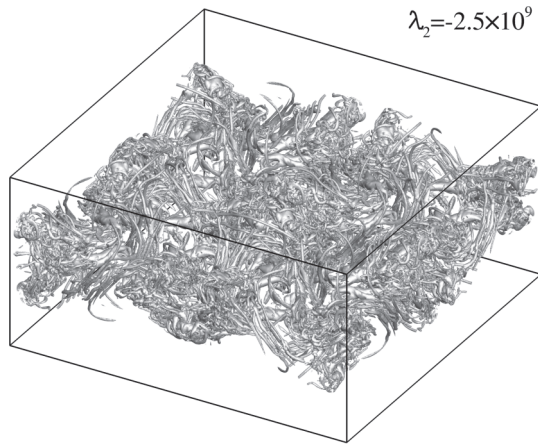


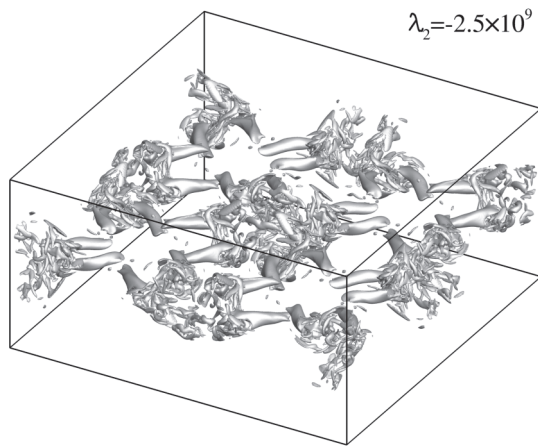
FIG. 5. Temporal evolution of dissipation, ε , for EE and NSE on different grid resolutions.

in Brachet *et al.* [36] data, we attribute its origin to the grid resolution.

(v) At late time, the decay rate on the fine grids does not match the DNS. It is quite likely that may be a history effect whereby the late-time behavior is contaminated by the residual effects of the unphysical transition; however, it underlines



(a) EE.



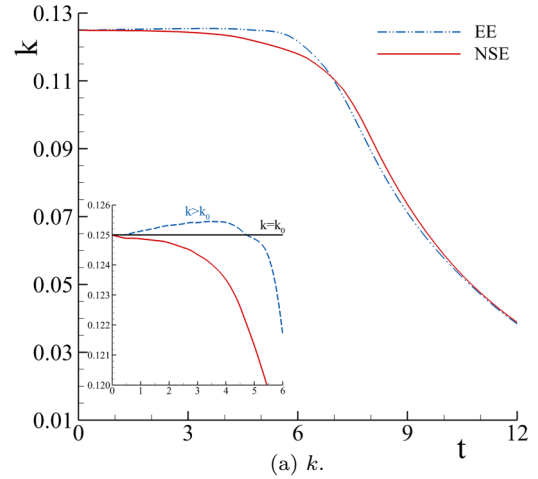
(b) NSE.

FIG. 6. Vortical structures of the TGV flow for EE and NSE on $N_c = 512^3$ at $t = 7$. Structures identified with the λ_2 criterion [83].

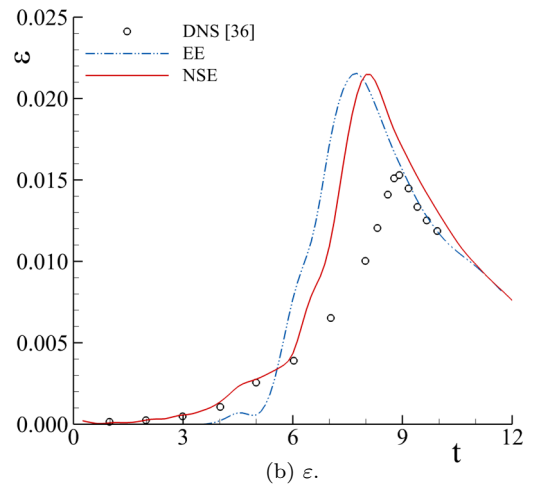
the fact that failure to capture the viscous effects may impact predictions even in the fully turbulent region.

NSE simulations, on the other hand, lead to distinct temporal evolutions of ε that are in close agreement with the reference data [36,38]. During the first nine time units, the discrepancies between predictions and DNS data are negligible, as well as the differences between solutions obtained with the three finest grids. At $9 \leq t \leq 11$, the discrepancies grow, but the solutions are still in good agreement with the DNS data, particularly to those of Drikakis *et al.* [38]. Considering the excellent agreement with these compressible simulations, we attribute the small discrepancies between our predictions and Brachet *et al.* [36] to compressibility effects. After this period, the magnitude of ε starts decreasing, and it is possible to identify a small second peak. This phenomenon is likely the consequence of suboptimal grid resolution at these late times [84].

Overall, the results of Figs. 3 and 5 show the limitations of the EE to predict transition in the TGV. Although it is expected that this flow will become Reynolds number independent as sufficiently high Re, it is clear that this has not yet occurred



(a) k .



(b) ε .

FIG. 7. Temporal evolution of kinetic energy, k , and dissipation, ε , for viscous (NSE) and inviscid (EE) RANS BHR-2 simulations on the finest grid.

even at $Re = 5000$ [85]. At the current Reynolds number of 3000, the results are Reynolds number dependent [36], and the EE cannot capture that. In clear contrast, ILES using the NSE achieves an excellent agreement with the DNS data, and the solutions converge upon grid refinement. It is important to note that although the EE and NSE solutions obtained in the coarsest resolution possess some similarities due to the magnitude of the numerical diffusion, these results exhibit a poor agreement with the DNS data.

Before investigating the physics behind the results of Figs. 3 and 5, we analyze the effect of viscosity to simulations using mathematical formulations modeling the entire turbulent field. Toward this end, an extra set of calculations is conducted with the viscous and inviscid RANS equations. These RANS computations run for at least 12 time units in grid resolutions ranging from $N_c = 128^3$ to 512^3 . The turbulence field is modeled through the Besnard-Harlow-Rauenzahn (BHR) multiequation RANS model [86] in the BHR-2 closure version [87].

The temporal evolution of the averaged total kinetic energy, k , and dissipation, ε , obtained in the finest grid resolution is depicted in Fig. 7. The results for the NSE show that the

temporal evolution of k and ε is identical to that predicted by ILES (see Figs. 3 and 5) and DNS [36] until $t \approx 6$. After this instant, the well-known limitations of RANS predicting transitional flows [88] lead to the overprediction of turbulence and, consequently, of ε . For this reason, the peak of ε is 50.2% larger than that obtained with ILES. The inviscid RANS calculations exhibit a similar peak. Furthermore, the assumption of inviscid fluid shifts the RANS prediction in the same manner observed for the ILES. This stems from the growth of the effective Reynolds number (see Sec. III A 1), and demonstrates that the assumption of inviscid fluid also affects formulations modeling the entire spectrum of turbulence scales. Although not exhibited, the outcome of grid refinement studies indicates that the apparent small shift between EE and NSE solutions at $t > 6$ might be a coincidence. The results of the two models on the two coarsest grids exhibit significant differences for $t \leq 20$.

1. Numerical Reynolds number

One of the consequences of assuming inviscid fluid is the inability to set the effective Reynolds number, Re_e , of the simulations. This stems from the fact that the effective viscosity of the computations becomes determined by its numerical component. Since the magnitude of the numerical viscosity is grid dependent, Re_e also varies upon grid refinement. This feature poses challenges to prediction and validation.

To evaluate the impact of this aspect on the computations' accuracy, this section assesses the magnitude of the numerical Reynolds number, Re_n , for viscous and inviscid simulations. This quantity is estimated using the method proposed by Zhou *et al.* [89] for decaying turbulent flow. The numerical viscosity, ν_n , is defined as the ratio between the magnitude of the averaged observed dissipation, ε , and the enstrophy, Ω :

$$\nu_n = \frac{\varepsilon}{\Omega}. \quad (20)$$

In Eq. (20), ε is given by Eq. (19) (without normalizing k), and

$$\Omega = \frac{1}{2} \frac{\overline{\rho\omega\omega}}{\bar{\rho}}, \quad (21)$$

where ω is the magnitude of the vorticity vector,

$$\boldsymbol{\omega} = \nabla \times \mathbf{V}, \quad (22)$$

and bold symbols denote vectors. Then, Re_n is defined as

$$Re_n \equiv \frac{V_o L_o}{\nu_n}. \quad (23)$$

It is important to highlight that the effective and numerical Reynolds numbers, Re_e and Re_n , are equivalent for ILES using the EE because $\nu = \nu_t = 0$ [see Eq. (10)]. This property does not hold for ILES using the NSE since ν is not assumed to be equal to zero.

Figure 8 depicts the temporal evolution of the ratio between the Re_n for inviscid and viscous calculations on grids $N_c = 128^3$ to 512^3 (the grid with $N_c = 1024^3$ is only used to calculate k and ε). Since Eq. (20) assumes turbulence decay [89], Fig. 8 only considers the interval $9 \leq t \leq 20$. As expected, the results indicate that $(Re_n)_{EE}/(Re_n)_{NSE}$ is closely dependent on the grid resolution. Whereas this ratio is approximately constant and equal to 1.4 for the coarsest grid, its magnitude

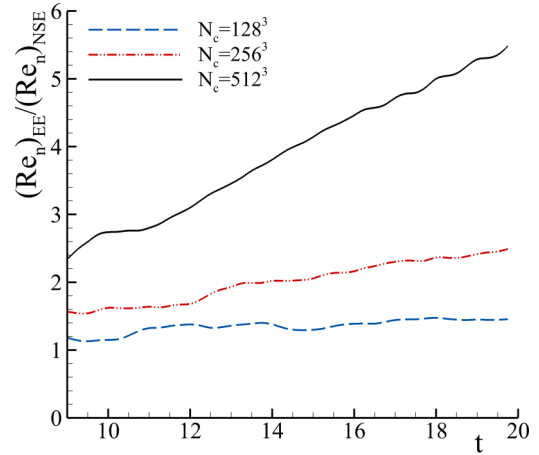


FIG. 8. Temporal evolution of the numerical Reynolds number, Re_n , for EE and NSE on different grid resolutions.

ranges from 2.8 to 6.0 for the finest grid resolution. This tendency indicates that the numerical Reynolds number of the EE calculations grows more rapidly than that of the NSE. Unlike $(Re_n)_{EE}$, $(Re_n)_{NSE}$ converges upon grid refinement.

Yet, more important than the observed growth in Re_n for the EE, one needs to understand the reason for this outcome. Since V_o and L_o are constants, $(Re_n)_{EE}/(Re_n)_{NSE}$ is determined by ν_n . This quantity, in turn, is calculated as the ratio between the flow dissipation and enstrophy plotted in Figs. 5 and 9. From these figures, it is possible to infer that the growth of $(Re_n)_{EE}/(Re_n)_{NSE}$ is essentially caused by a significant increase of the enstrophy of the EE simulations upon grid refinement. Lacking physical dissipation, the EE simulations will continue to give rise to increasingly small scale fluctuations as the grid is refined. Consequently, the vorticity field predicted by the EE is more intense than for the NSE at the specified Re , and may possess different features.

2. Vorticity field

The results of Figs. 8 and 9 demonstrate the strong impact of viscosity on the magnitude and dynamics of the vorticity

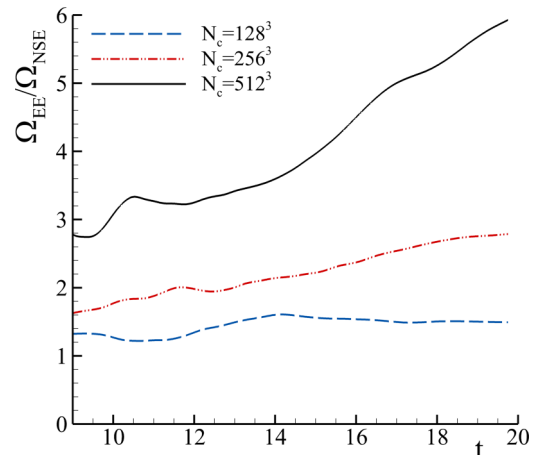


FIG. 9. Temporal evolution of the enstrophy magnitude, Ω , for EE and NSE on different grid resolutions.

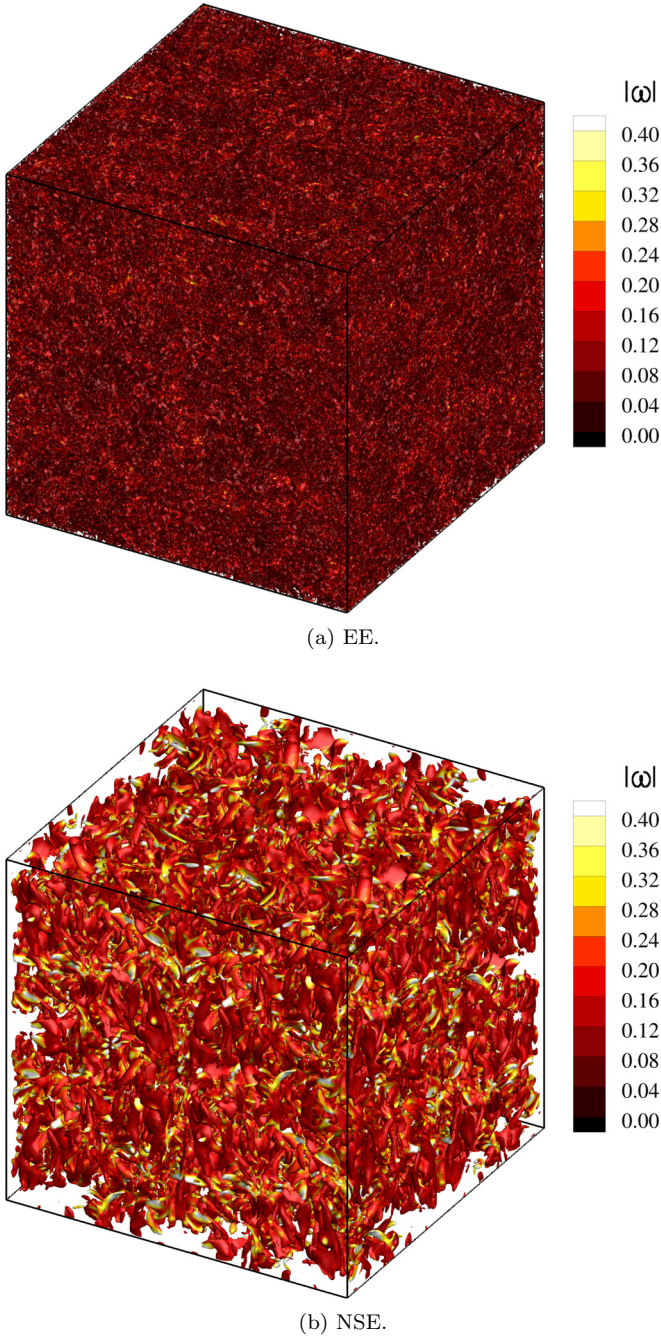


FIG. 10. Isosurfaces of the normalized x_3 vorticity field ($|\omega_3| = 1.7$) colored by the vorticity magnitude for distinct models: results at $t = 20$ with $N_c = 512^3$.

field. To illustrate the effect of assuming inviscid flow on the vorticity magnitude, Fig. 10 depicts the isosurfaces of the normalized vertical vorticity field at $t = 20$ predicted with the EE and NSE. The structures are colored by the vorticity magnitude normalized by its maximum value. The plots confirm that inviscid calculations predict larger magnitudes of vorticity and, consequently, finer-scale structures than the NSE. The results also show that the NSE lead to a more homogeneous vorticity field due to the broader coloring range of the structures (normalized by maximum value $|\omega_3|_{\max}$).

The consequences for the vorticity dynamics of assuming inviscid fluid can be evaluated quantitatively by studying the mechanisms contributing to the production and diffusion of vorticity: stretching, \mathcal{T}_S ; dilatational, \mathcal{T}_D ; baroclinic, \mathcal{T}_B ; and viscous, \mathcal{T}_V . The first two processes account for the stretching of vorticity [90,91] due to velocity gradients and compressibility effects. The baroclinic mechanism describes the evolution of vorticity due to the misalignment of the pressure and density gradients, whereas the viscous mechanism accounts for the diffusion of vorticity due to viscous effects. The temporal evolution of vorticity can be best described by the following equation [92,93]:

$$\frac{D\omega_i}{Dt} = \mathcal{T}_{S_i} - \mathcal{T}_{D_i} + \mathcal{T}_{B_i} + \mathcal{T}_{V_i}, \quad (24)$$

where

$$\mathcal{T}_{S_i} = \omega_j \frac{\partial V_i}{\partial x_j}, \quad (25)$$

$$\mathcal{T}_{D_i} = \omega_i \frac{\partial V_j}{\partial x_j}, \quad (26)$$

$$\mathcal{T}_{B_i} = e_{ijk} \frac{1}{\rho^2} \frac{\partial \rho}{\partial x_j} \frac{\partial P}{\partial x_k}, \quad (27)$$

$$\mathcal{T}_{V_i} = e_{ijk} \frac{\partial}{\partial x_j} \left(\frac{1}{\rho} \frac{\partial \sigma_{km}}{\partial x_m} \right). \quad (28)$$

The viscous term only appears on the NSE, not the EE. Figure 11 shows the temporal evolution of the magnitude of these mechanisms for viscous and inviscid computations upon grid refinement. The baroclinic term is not shown, due to its minimal importance for the present flow problem, $\mathcal{T}_B/\mathcal{T}_S \leq 3\%$ ($N_c = 512^3$). The data are normalized by the magnitude of \mathcal{T}_{S_i} since this term is expected to govern the right-hand side of Eq. (24).

Both the stretching and the viscous terms represent phenomena that are not fully resolved in ILES, and which therefore increase in magnitude with grid refinement. However, as dissipation is a small scale process, whereas stretching is dominated by the larger scales, the ratio of these terms should increase as the grid is refined. This can be seen in Fig. 11, where $\mathcal{T}_V/\mathcal{T}_S$ reaches 19.0 and 73.9% at $t = 5$ and 20 for the finest grid ($N_c = 512^3$). This reiterates the importance of viscous effects in the TGV, and further explains the discrepancies between EE and NSE solutions. The increased relevance of \mathcal{T}_V upon grid refinement is likely caused by the reduction of the simulations' numerical diffusion.

The ratio $\mathcal{T}_D/\mathcal{T}_S$ remains approximately constant for the EE. It can reach 16.0% for $N_c = 512^2$, demonstrating that compressibility effects are relevant for simulations using this mathematical model. In contrast, the NSE results indicate that $\mathcal{T}_D/\mathcal{T}_S$ reduces by a factor of 2 with the grid, reaching a maximum value of 7.5% for $N_c = 512^3$.

3. Spectral features

Figure 12 compares the temporal evolution of the kinetic energy spectrum of both models at time instants after the peak of dissipation, once the flow is turbulent. The spectra for the (numerical-diffusion constrained) nominally inviscid ILES-EE calculations exhibit a longer inertial range—associated

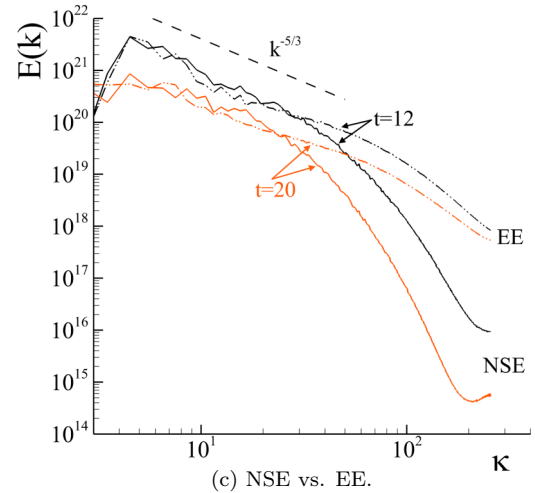
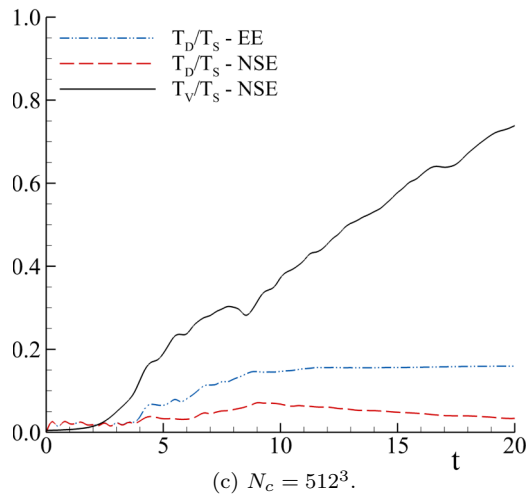
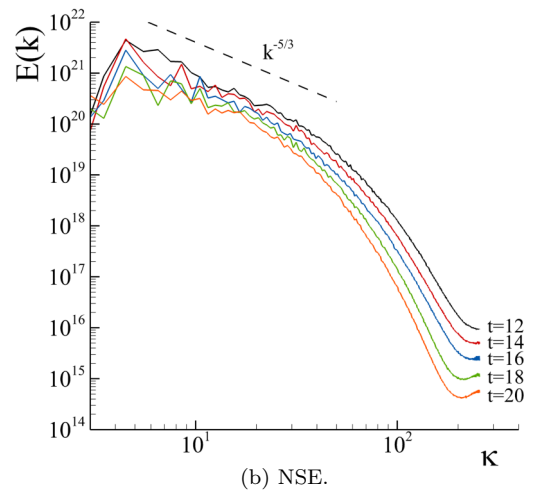
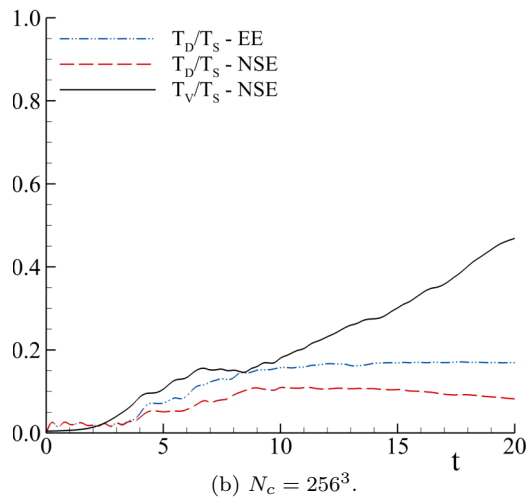
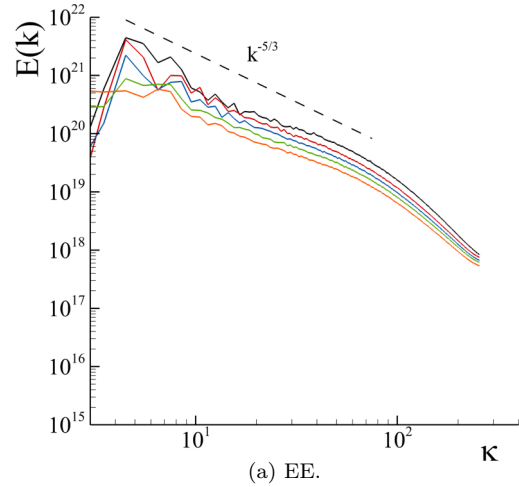
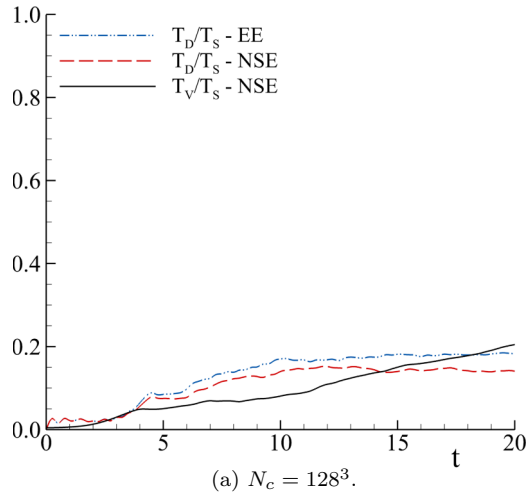


FIG. 11. Temporal evolution of the norm of the vorticity equation terms (\mathcal{T}_S , \mathcal{T}_D , and \mathcal{T}_V) for EE and NSE.

FIG. 12. Temporal evolution of the turbulence kinetic energy spectrum, $E(k)$, for EE and NSE. Grid resolution is $N_c = 512^3$.

with a resolution-dependent Re_e —and show absence of a clear viscous subrange. Also apparent in the spectra for the EE case is a suggested power law shallower than Kolmogorov’s in the near-dissipation region (the so-called bottleneck effect); the latter is commonly observed in very high-Re DNS predictions and laboratory observations, and recognized to be a feature

of the NSE solutions for high (but finite) Re . In contrast, the spectra of the NSE calculations, for which we can prescribe a lower Re of 3000, present a significantly more rapid energy decay with k at later times, and show a clear distinction between the inertial and viscous subranges.

TABLE II. Computational cost in CPU hours of EE and NSE computations for different grid resolutions.

Grid	t_{EE} (CPU.h)	t_{NSE} (CPU.h)	t_{NSE}/t_{EE}
512^3	302, 194	322, 284	1.07
256^3	16, 057	17, 962	1.12
128^3	1, 144	1, 204	1.05

4. Computational cost

The analysis of the TGV concludes with the assessment of the computational cost of the two mathematical models. This is important in order to address one of the arguments driving the use of the EE instead of the NSE, the cost. Table II shows that the cost difference between the two models is typically around 10%, with the EE computationally less expensive. Considering the gain in accuracy, the additional cost of the NSE does not seem to justify the use of the EE.

B. Shocked gas curtain

The experiments of Balakumar *et al.* [37] consist of a varicose gas curtain impacted by an initial shock, which triggers initial disturbance growth. This enhances the mixing of the different materials and leads to the development of the characteristic Richtmyer-Meshkov instability and coherent structures. Subsequently the mixing region is impacted by a second shock (reshock) which ultimately promotes transition

to turbulence. The temporal evolution of the gas curtain is illustrated in Fig. 13. This figure compares the predictions of the EE and NSE on grid g_3 against the experiments of Balakumar *et al.* [37]. In this figure, the gas curtain is measured by the concentration intensity of SF_6 , I_{SF_6} :

$$I_{SF_6} \equiv \frac{c_{SF_6}}{(c_{SF_6})_{max}}, \tag{29}$$

where c_{SF_6} is the local mass concentration of SF_6 in the mixture, and $(c_{SF_6})_{max}$ is its maximum value. Except at $t = 0$, the experimental results were measured $5 \mu s$ before the predictions. Although such a time lag can make the comparison between experiments and predictions at time instants close to the two shocks more difficult, it does not affect the assessment of the influence of molecular viscosity and diffusivity effects to the predictions. To be consistent with Balakumar *et al.* [37], all numerical measurements shown in this section are taken at plane $x_3 = 20$ mm.

The results of Fig. 13 show a close agreement between numerical and experimental measurements until reshock, $t = 600 \mu s$. At $t = 0$, the perturbed gas curtain is at rest and the shock wave is about to strike its upstream interface. The passage of the shock wave compresses the curtain ($t = 20 \mu s$), and deposits vorticity through baroclinic processes. This triggers the mixing of the different materials. Next, the downstream interface of the gas curtain undergoes a phase inversion, whereas its upstream interface starts growing ($t = 40 \mu s$). In the following instants ($t \leq 220 \mu s$), the curtain develops a symmetric and sinusoidal form, where projectiles

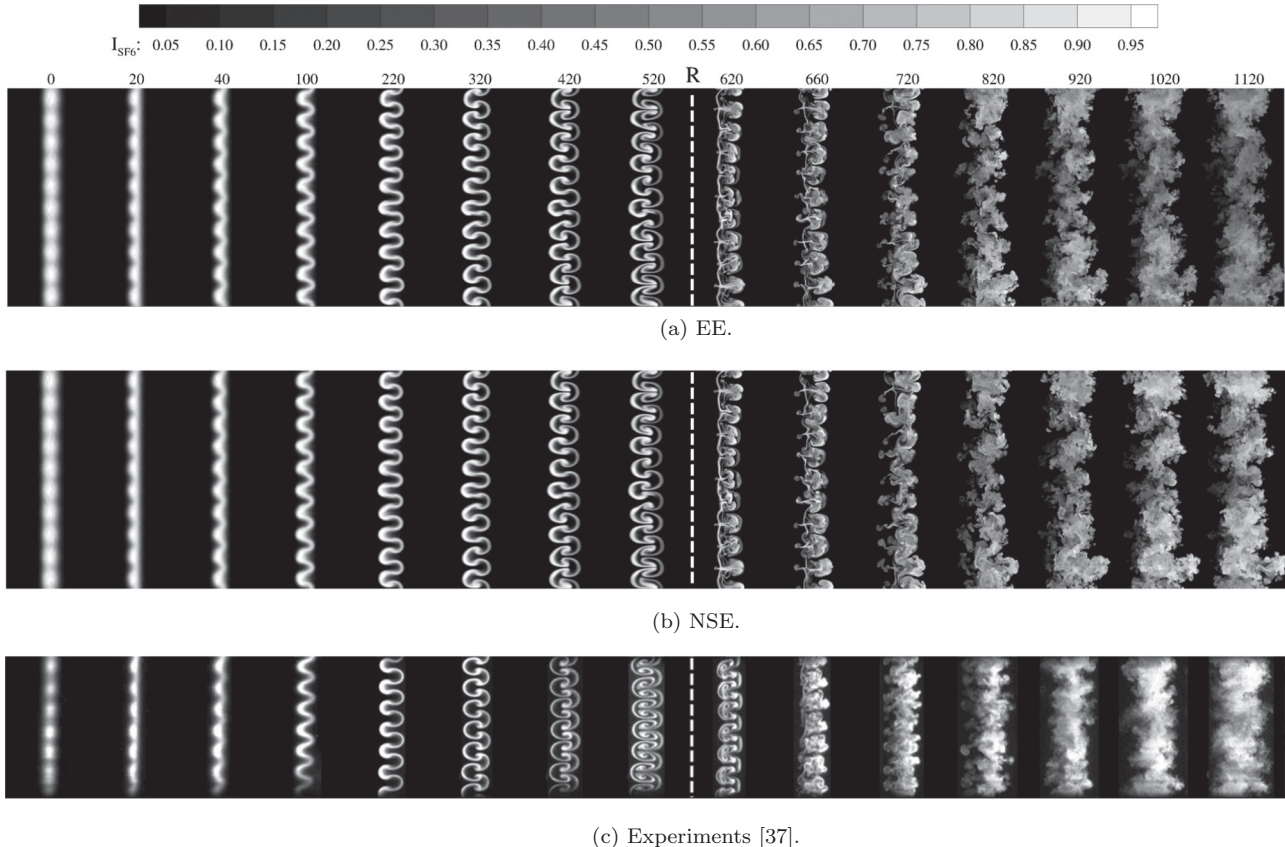


FIG. 13. Temporal evolution of the SF_6 intensity, I_{SF_6} , for EE and NSE on the finest grid. Experiments are taken from Balakumar *et al.* [37].

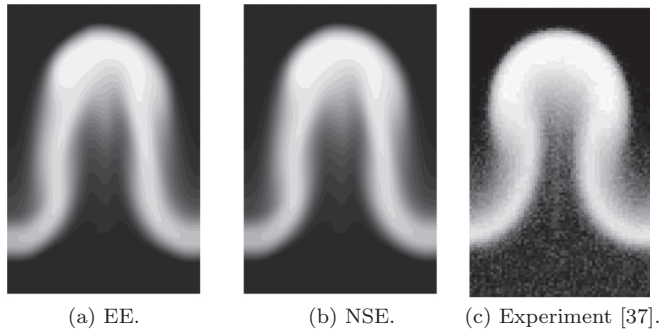


FIG. 14. Visualization of the Richtmyer-Meshkov structure and projectiles at $t = 220 \mu s$ for EE and NSE on the finest grid. Experiments are taken from Balakumar *et al.* [37].

ject from the primary structure (Fig. 14). At this time, the bridges connecting different jets start getting thinner. In addition, the interfaces of the gas curtain start to roll up, leading to the generation of counter-rotating vortices with the characteristic mushroomlike shape of the Richtmyer-Meshkov coherent structure. These structures lose some of their symmetry at late times ($t \leq 520 \mu s$). Despite the good agreement between simulations and experiments until reshock, it is still possible to identify some discrepancies at late times. Figure 13 shows smaller experimental asymmetries in the Richtmyer-Meshkov structures than for the simulations. This likely stems from differences between the numerical and experimental initial flow conditions [24,54], which are those given in [37,54]. Comparing the two models, the results exhibit negligible differences between inviscid and viscous calculations (for the three grid resolutions tested).

The reflected shock wave passes through the gas curtain at $t = 600 \mu s$. The experiments indicate that the reshock increases the mixing of the different materials, and leads to a rapid spatiotemporal development of the flow. At $620 \mu s$, the bridges connecting neighboring jets become flatter and the mixing-layer width reduces due to compressible effects. In the following instants, the mixing layer expands and the mixing rate increases. Also, it is possible to observe projectilelike structures ejecting from the mixing layer ($t \leq 820 \mu s$). At later times, the mixing layer starts exhibiting high intensity turbulence features, becoming a homogeneous mixture with a characteristic cloudlike structure.

During this period, the numerical simulations exhibit an overall good agreement with the experiments. Nevertheless, it is still possible to identify some discrepancies in solutions obtained at time instants just after reshock. Once again, these mismatches are most likely caused by the time lag between experimental and numerical measurements, and the undercharacterization of the experimental initial conditions [9,54,94]. The comparison of the two mathematical models shows negligible qualitative differences until $t = 920 \mu s$. After this instant, the composition of the mixing layer predicted with the two models starts exhibiting meaningful differences. Whereas the EE predict small intensities of c_{SF_6} , I_{SF_6} , the NSE lead to larger values of this quantity. These are in significantly better agreement with the experiments. Note that all intermediate values of I_{SF_6} with EE are entirely

due to subgrid processes via the numerical diffusion, as there is no molecular diffusion term in the equations.

To investigate these differences, Fig. 15 depicts the volumetric fraction of mixture possessing values of c_{SF_6} within seven ranges. These vary from $0 \leq c_{SF_6} < 0.10$ to $0.60 \leq c_{SF_6} < 0.70$. It is important to emphasize that the homogeneity of the mixture enhances with the reduction of c_{SF_6} . Considering the finest grid, Figs. 15(a) to 15(c), the results indicate that the NSE improve the homogeneity of the mixture. In general, viscous computations tend to homogenize the mixing layer by reducing the flow regions with larger concentrations of SF_6 , thus increasing the fraction of the mixture where $c_{SF_6} < 0.10$. At $t = 1120 \mu s$, for example, c_{SF_6} is below 0.10 in 38.8% of the mixing layer predicted with the EE, whereas this value grows to 43.2% for the NSE. The data also show that at $t = 1020$ and $1120 \mu s$, only the EE lead to values of c_{SF_6} above 0.5 and 0.4, respectively. These results explain the observed differences in I_{SF_6} , and demonstrate that inviscid calculations can have a significant impact on the composition of the mixture. As expected, the importance of diffusivity effects diminishes for g_2 due to numerical diffusion. This behavior is observed in Figs. 15(d)–15(f) and 16, where it is possible to infer that the magnitude of I_{SF_6} is similar for EE and NSE computations.

The temporal evolution of the mixing-layer width, w , predicted by both models on g_3 and g_2 is depicted in Fig. 17. This quantity is defined as follows. Prior to reshock ($t < 600 \mu s$), the mixing-layer width is defined as the largest distance between the upstream and downstream points of each structure where the volume fraction of SF_6 , f_{SF_6} , exceeds 5%. The values obtained for each wavelength are then spatially averaged. After reshock ($t \geq 600 \mu s$), the mixing-layer width is estimated using the same procedure but without averaging over each wavelength. Instead, the final mixing-layer width results from averaging the value of w computed at each transverse plane. In contrast to the simulations, the projectilelike structures observed after reshock are not considered in the experimental measurements of w .

Figure 17 shows again the close agreement between experiments and simulations until reshock. After reshock, however, the numerical simulations on g_3 overpredict w . This result stems from the aforementioned mismatches between numerical and experimental initial flow conditions [9,24,54,94]. Comparing EE to NSE, the data indicate that the predictions of w are similar until $t = 1000 \mu s$. After this instant, it is possible to identify discrepancies between the results of the two models. These are caused by c_{SF_6}/f_{SF_6} variations in the mixture (Fig. 15). Similar to the results of Fig. 16, the values of w obtained on the coarsest grids are less sensitive to the model due to numerical diffusion.

Next, we turn our attention to the temporal evolution of the flow kinetic energy:

$$k = \frac{1}{2}(v_1^2 + v_2^2 + v_3^2). \quad (30)$$

In Eq. (30), v_i is the fluctuating velocity, which is calculated as the difference between the instantaneous, V_i , and the spatial (along transverse direction) mean, \bar{V}_i , velocities. The kinetic energy distribution across the mixing zone at four instants is presented in Fig. 18.

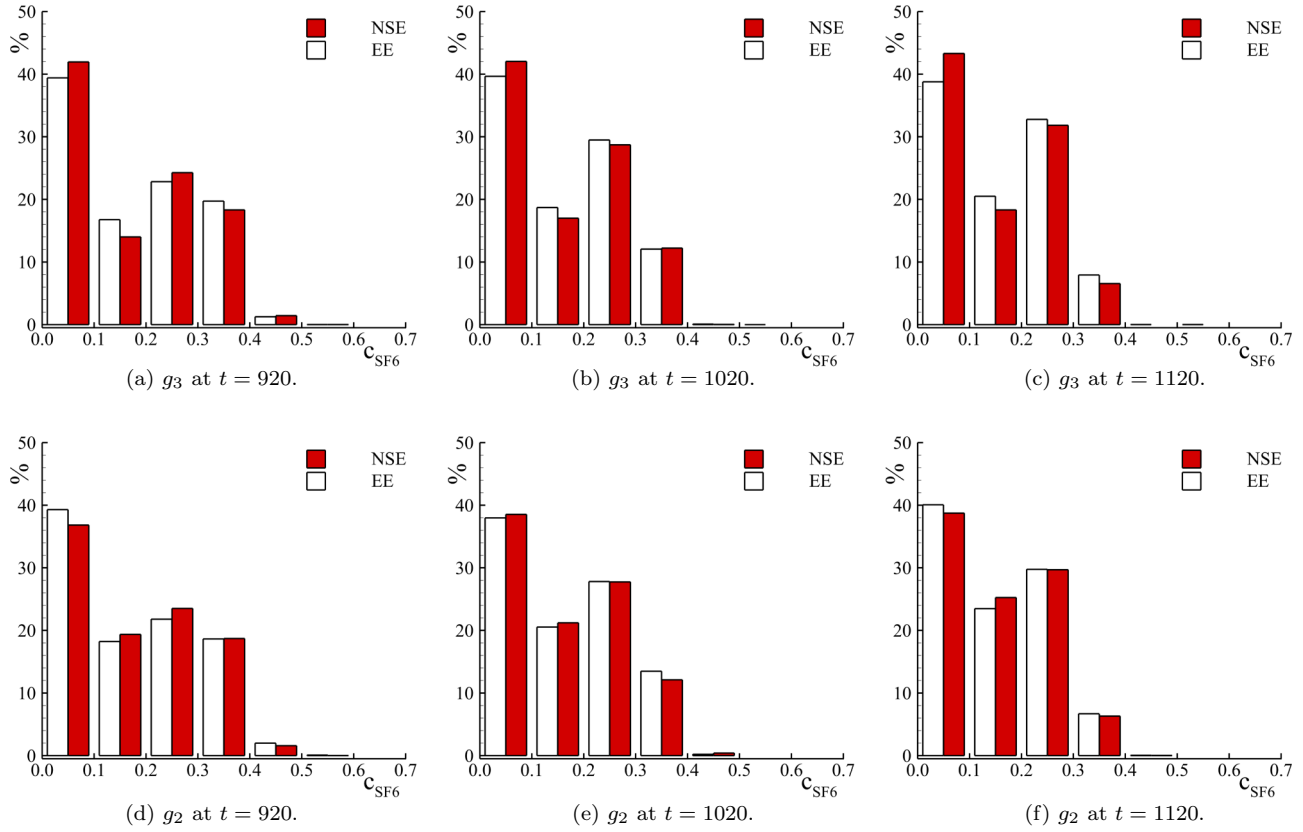


FIG. 15. Fraction of the gas curtain with a local mass concentration of SF₆, c_{SF_6} , within selected ranges for EE and NSE at different time instants and grid resolutions.

At $t = 700 \mu s$, both models predict profiles of kinetic energy exhibiting two peaks. The first, located at $x_1 \approx 50.75 \text{ cm}$, is caused by the projectilelike structures observed in Fig. 13, whereas the second coincides with the center of the mixing layer ($x_1 \approx 51.05 \text{ cm}$). The NSE has a smoother profile and larger peaks of k compared with the EE. For this reason, k_{\max} predicted by the NSE is 4% larger than that predicted by the

EE. In the following instants, the magnitude of k reduces for both models. From $t = 700$ to $1000 \mu s$, k_{\max} decreases 84.4% for the EE and 82.7% for the NSE. Furthermore, the profiles start becoming symmetric, evidence of an enhancement in the mixing-layer homogeneity. Yet, the most significant result in Fig. 18 is the fact that k_{\max} at $t = 1000 \mu s$ predicted by the NSE is 16.4% larger than for the EE. Since the magnitude

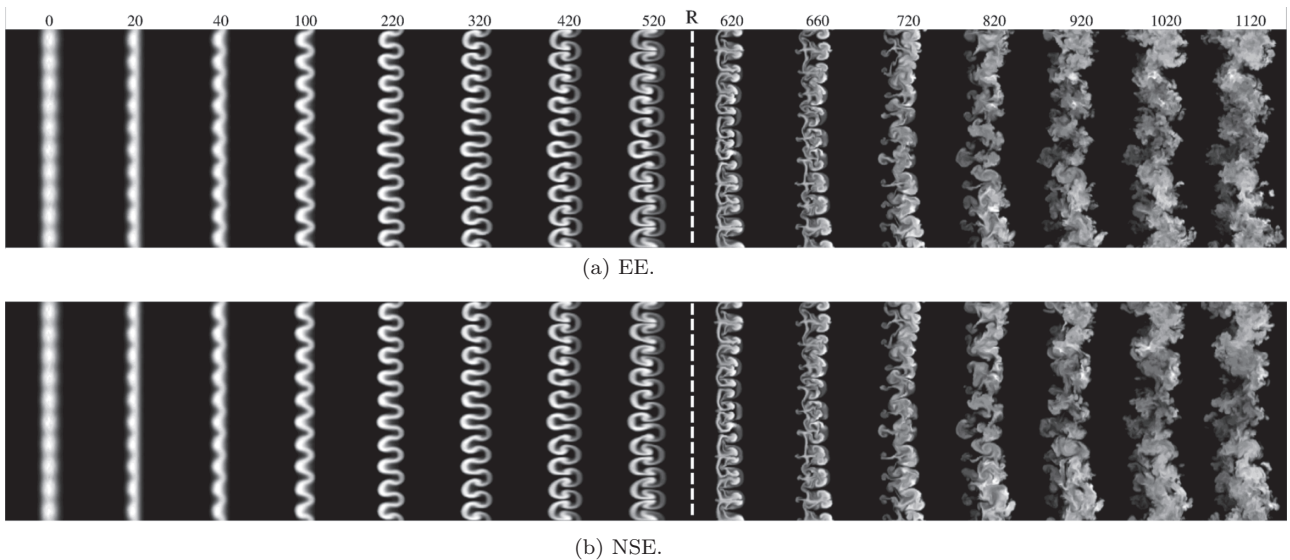


FIG. 16. Temporal evolution of the SF₆ intensity, I_{SF_6} , for EE and NSE on g_2 .

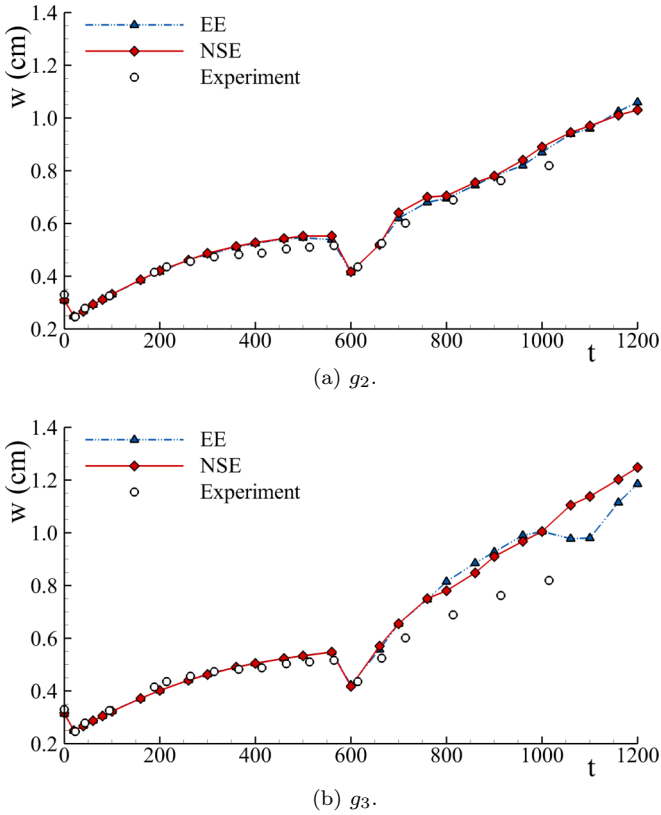


FIG. 17. Temporal evolution of the mixing-layer width, w , for EE and NSE on different grid resolutions. Experiments are taken from Balakumar *et al.* [37].

of k strongly influences the mixing rate, these results underscore the importance of molecular viscosity and diffusivity phenomena to shock-driven turbulent mixing. The growth of k observed in NSE calculations is also connected to an increase in the flow Mach number. It was observed that the instantaneous averaged values of the Ma can exceed by 11% those obtained with the EE (considering the time instants of Fig. 17).

The importance of viscous effects is also observed in the variance of c_{SF_6} , $\text{var}(c_{\text{SF}_6})$, depicted in Fig. 19. This presents the results as the percent difference between $\text{var}(c_{\text{SF}_6})$ predicted with NSE and EE along the mixing layer ($0 \leq x_w/w_{\text{NSE}} \leq 1$) at three instants after reshock. Figure 19 also includes the line w_{EE} which represents the relative mixing-layer location predicted by the inviscid calculation. The numerical results indicate that the magnitude of $\text{var}(c_{\text{SF}_6})$ of the viscous calculation can be significantly larger than that of the inviscid computation. It is observed that these differences can reach 25%. This result stems from viscous effects that enhance material mixing, and the higher turbulence intensities of viscous simulations shown in Fig. 18. Also, it is important to emphasize that mixing in EE simulations is only possible due to numerical diffusion. Figure 19 also indicates that the differences in w verified in Fig. 17 between NSE and EE calculations are mostly driven by the left interface (w_{EE}). Whereas the right interface of the mixing layer predicted with the EE is at $x_w > 0.97w_{\text{NSE}}$, the left one can reach $x_w = 0.10w_{\text{NSE}}$.

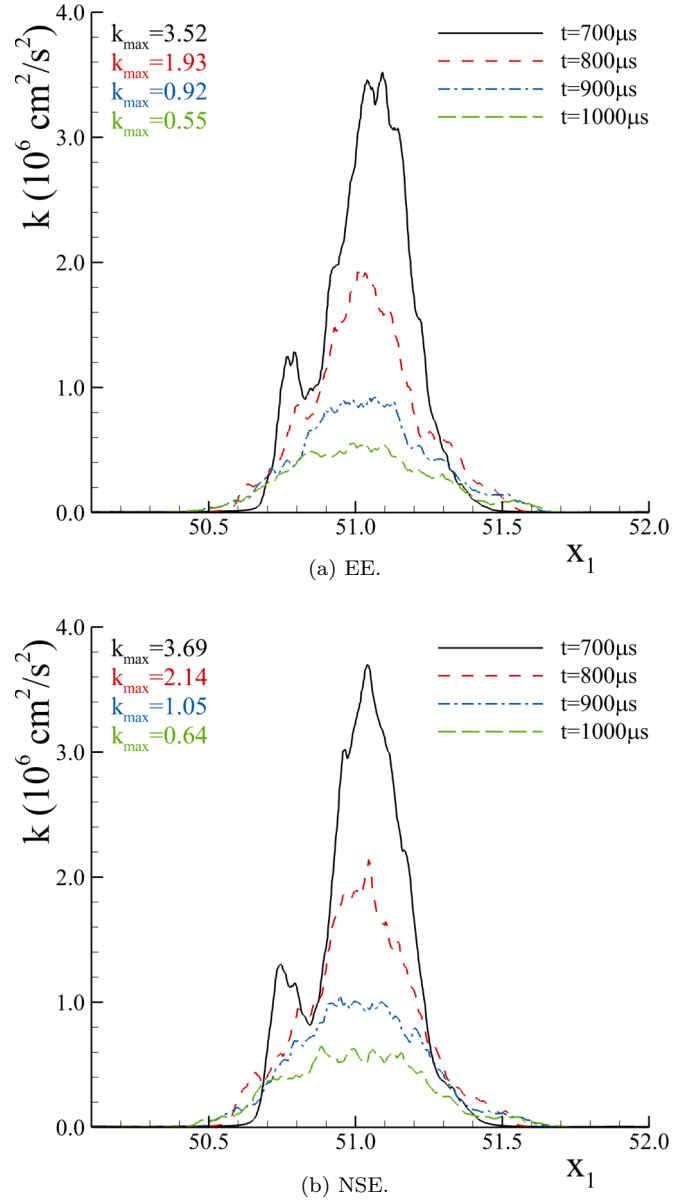


FIG. 18. Temporal evolution of the flow kinetic energy, k , for EE and NSE on g_3 .

1. Numerical Reynolds number

Figure 20 presents the temporal evolution of the numerical Reynolds number, Re_n , for viscous and inviscid computations on the finest grid. For this problem, Re_n is estimated through the method proposed by Zhou *et al.* [89] as in the derivation leading to Eq. (30) in Grinstein *et al.* [95]:

$$\text{Re}_n = \frac{6w^2}{k} S_{ij} S_{ij}. \quad (31)$$

In this relation, w is the mixing-layer width presented in Fig. 17, k is the flow kinetic energy, and S_{ij} is the strain-rate tensor. Here, k and S_{ij} consider the complete velocity field (mean, coherent, and turbulent [96,97]) so that the estimated Re_n represents an upper limit for its magnitude.

As expected, Fig. 20 indicates that Re_n increases in time and upon grid refinement. Whereas the first stems from the

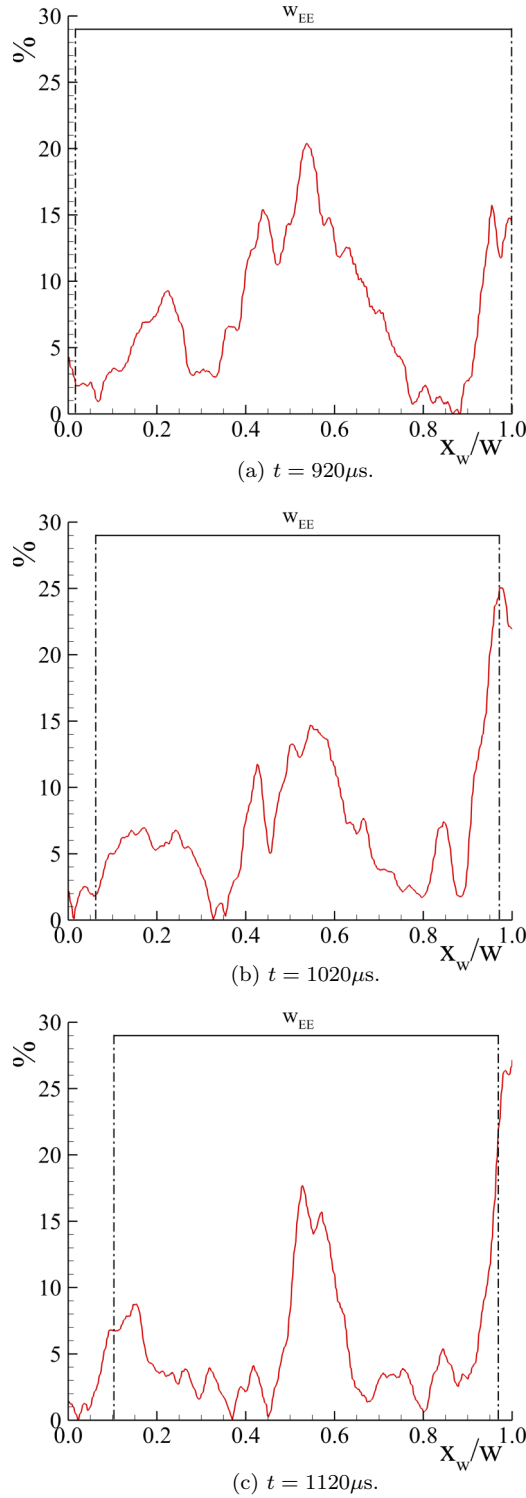


FIG. 19. Difference between the variance of c_{SF_6} , $\text{var}(c_{SF_6})$, for NSE and EE on g_3 at different instants. Results are shown as a percentage of $[\text{var}(c_{SF_6})]_{EE}$.

growth of the strain-rate tensor magnitude in time due to flow unsteadiness, the second originates from the reduction of numerical diffusion with the grid refinement. The data also show that these differences are amplified after reshock, and can reach 17.0% for g_2 and 34.5% for g_3 . Naturally, the

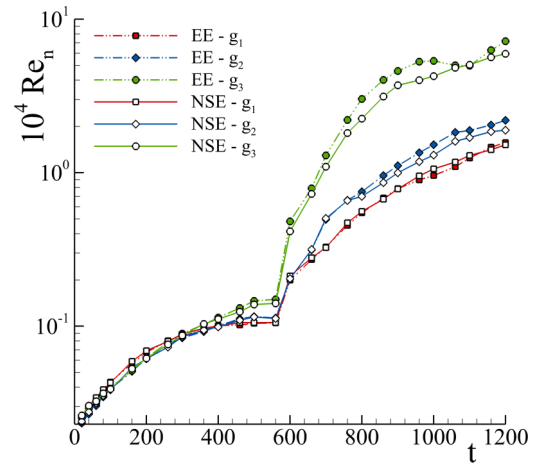


FIG. 20. Temporal evolution of the numerical Reynolds number, Re_n , for EE and NSE on different grid resolutions.

largest values of Re_n are achieved by inviscid calculations. At $t = 1200 \mu s$, $(Re_n)_{EE} = 7.2 \times 10^4$. This value clearly exceeds the critical mixing transition, Re_c , proposed by Dimotakis [27] ($Re_c \geq 1.0\text{--}2.0 \times 10^4$), and shows the impact of viscous effects on solutions at Re higher than for the TGV. The results of Fig. 20 also illustrate that mismatches between $(Re_n)_{EE}$ and $(Re_n)_{NSE}$ start earlier as the grid refines.

2. Vorticity field

As previously demonstrated for the TGV, the dynamics of the vorticity field is closely dependent on molecular viscosity and diffusivity effects. Since the vorticity field has a strong impact on the physics of material mixing, Fig. 21 depicts the evolution of the vorticity magnitude for viscous and inviscid computations on the finest grid. The results reveal that the inviscid flow assumption leads to a meaningful increase in the vorticity magnitude. Although this tendency is visible before and after reshock, it is more pronounced after the mixing layer undergoes the second shock. During this period, ω_{EE} can exceed ω_{NSE} by 25.6%.

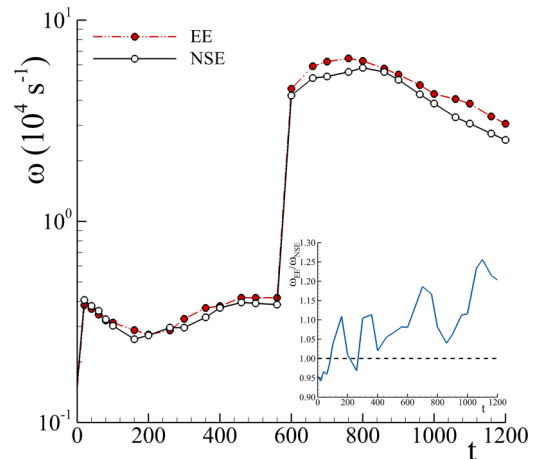


FIG. 21. Temporal evolution of the vorticity magnitude, ω , for EE and NSE on the finest grid.

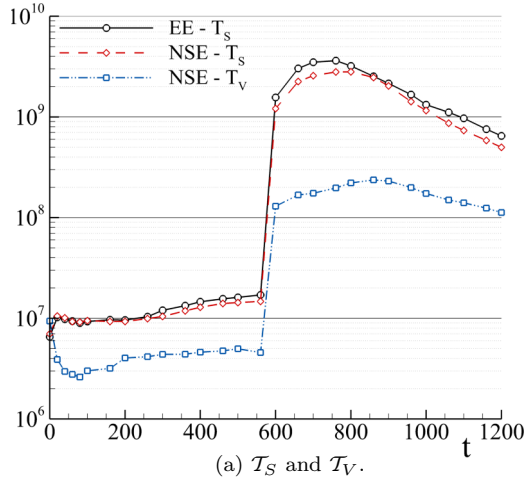
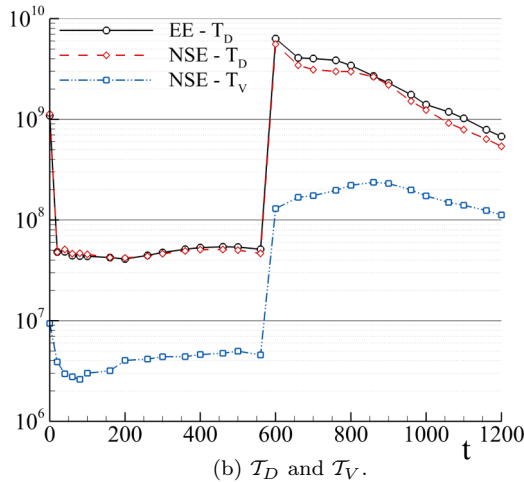
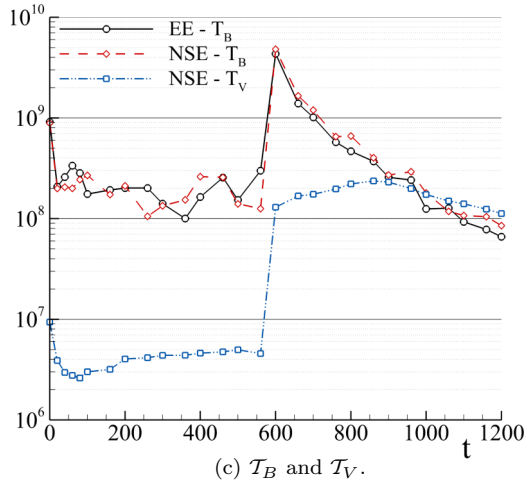
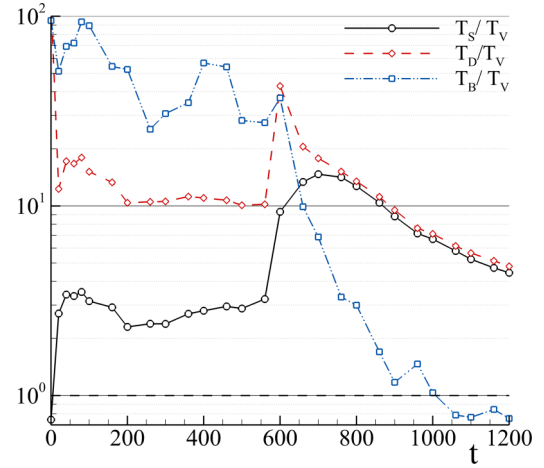

 (a) \mathcal{T}_S and \mathcal{T}_V .

 (b) \mathcal{T}_D and \mathcal{T}_V .

 (c) \mathcal{T}_B and \mathcal{T}_V .

 FIG. 22. Temporal evolution of the norm of the vorticity equation terms (\mathcal{T}_S , \mathcal{T}_D , \mathcal{T}_B , and \mathcal{T}_V) for EE and NSE on grid g_3 .

Despite the increase of ω , Figs. 13 and 15 have shown that the NSE enhance the homogeneity of the mixture. This shows the role of molecular viscosity and diffusivity to the predictions. To address this point, Figs. 22 and 23 present the evolution of the magnitude of the flow mechanisms responsible for the production and diffusion of vorticity: stretching, \mathcal{T}_S ; dilatation, \mathcal{T}_D ; baroclinic, \mathcal{T}_B ; and viscous, \mathcal{T}_V [Eqs. (25)–


 FIG. 23. Temporal evolution of the norm of the vorticity equation terms (\mathcal{T}_S , \mathcal{T}_D , \mathcal{T}_B , and \mathcal{T}_V) for NSE on grid g_3 .

(28)]. As observed in Pereira *et al.* [24], the results of both models illustrate that the baroclinic mechanism dominates the production of vorticity until reshock. Nevertheless, the magnitude of the dilatation and stretching processes is not negligible. On the other hand, the viscous mechanism does not exceed 4% of \mathcal{T}_B for NSE computations. The comparison of EE and NSE indicates that inviscid calculations lead to a small increase in \mathcal{T}_S and \mathcal{T}_D .

Upon reshock, $t \geq 600 \mu s$, \mathcal{T}_B experiences a rapid decay, whereas \mathcal{T}_S and \mathcal{T}_D experience a substantial growth. The latter result makes these two mechanisms the largest contributors to the production of vorticity. Regarding viscous effects, the results show that \mathcal{T}_V experiences a significant relative increase, which makes its magnitude represent more than 20% of \mathcal{T}_S or \mathcal{T}_D . Also, the magnitude of \mathcal{T}_V can surpass that of \mathcal{T}_B at $t > 1000 \mu s$. Along with the results of the previous sections and the fact that the present finest grid is adequate but not optimal for this problem [24], Figs. 22 and 23 reiterate the importance of molecular viscosity and diffusivity effects to the quality of the predictions. Figure 22 also shows that the differences between the various mechanisms predicted with EE and NSE increase after reshock. Whereas inviscid calculations lead to larger \mathcal{T}_S and \mathcal{T}_D , with values that can exceed 36.4 and 29.5% of those obtained with the NSE, \mathcal{T}_B predicted by the NSE is globally larger than by the EE.

3. Spectral features

Figure 24 depicts the turbulence kinetic energy spectrum for inviscid and viscous computations at various time instants after reshock. The spectra are calculated using solution points inside a 256^3 cubic domain located at the center of the mixing layer. This grid possesses a lower resolution than that used in the computations because we map the AMR grid onto a uniform grid. Similar to the TGV case, the results show that the inviscid assumption affects the turbulence field dynamics. It is visible that inviscid calculations lead to an earlier transition to turbulence due to the fact that the spectrum of the EE at $t = 700 \mu s$ contains a wider range of scales (wavelengths) than for the NSE. At late times, the spectra obtained with the EE also feature broader inertial ranges ($t \geq 1000 \mu s$). In fact,

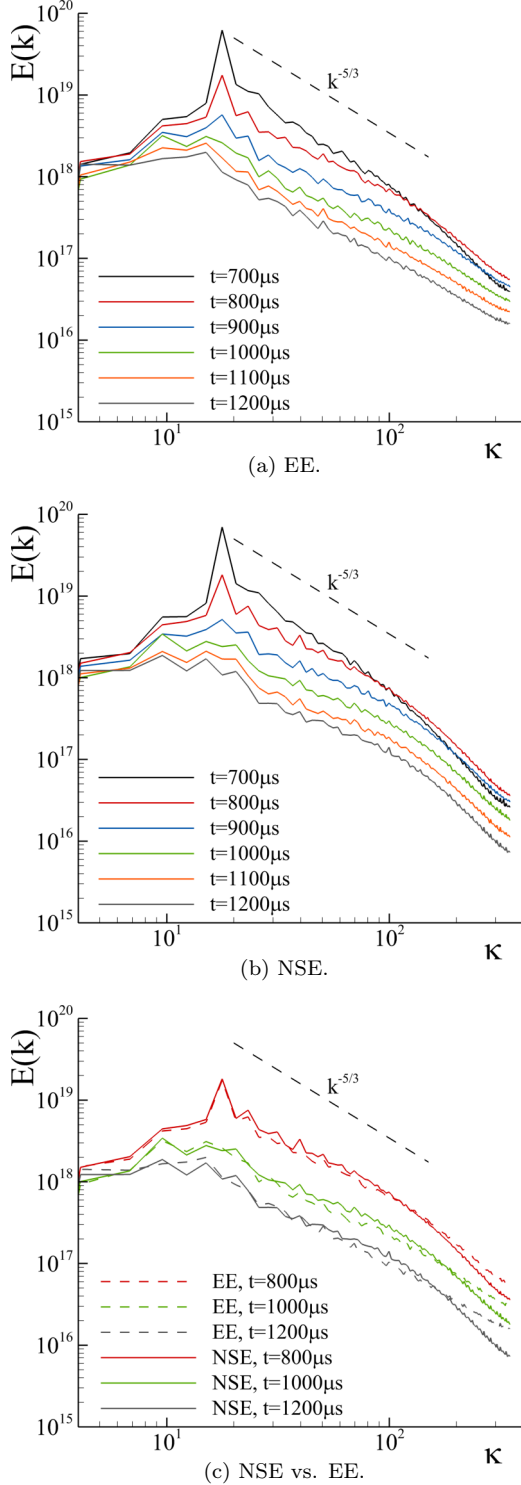


FIG. 24. Temporal evolution of the turbulence kinetic energy spectrum, $E(k)$, for EE and NSE on grid g_3 .

it is not possible to identify a dissipative subrange in the EE results. Differences in Re_e cause this outcome.

4. Computational cost

The discussion of the results concludes with the assessment of the simulations' computational cost. This is presented

TABLE III. Computational cost in CPU hours of EE and NSE computations for different grid resolutions.

Grid	t_{EE} (CPU h)	t_{NSE} (CPU h)	t_{NSE}/t_{EE}
g_3	380 328	156 699	0.41
g_2	26 766	12 493	0.47
g_1	2972	888	0.30

in Table III for the different grids. Despite the EE having fewer terms than the NSE and requiring larger time steps (Table I), the results indicate that inviscid calculations are at least 2.1 times more expensive than viscous simulations. To understand this result, Fig. 25 depicts the spatial resolution of g_3 at $t = 220 \mu s$ for both EE and NSE. The results show that when employed in EE calculations, the AMR algorithm refines the grid in larger areas of the domain, where the computations should not need fine grid resolutions. In addition to larger values of Re_e , this stems from the fact that inviscid calculations are not able to rapidly damp flow perturbations originating in the passage of the shock wave through the gas curtain. As a result, the gradients of pressure and density used as refinement criterion get steeper, increasing the the number of cells (Fig. 2) and, consequently, the computational cost of inviscid simulations. Viscous computations, on the other hand, rapidly dissipate such perturbations and so only refine the grid in the mixing-layer and shock-wave regions.

Although modified AMR algorithms may minimize this issue, the underlying problem will persist due to the inviscid fluid assumption, $\nu = 0$. In this manner, density and pressure perturbations created by the two shocks are not dissipated, thus leading to steeper flow gradients that AMR algorithms are designed to calculate accurately. Considering the impact of molecular viscosity and diffusivity effects in the accuracy and cost of the simulations, the viscous NSE seem to be the best approach to predict the present transitional shock-driven turbulent mixing flow.

IV. CONCLUSIONS

We investigated the importance of molecular viscosity and diffusivity effects on the prediction of transitional and shock-driven mixing flow problems that include high and low Re and Ma regions. Two representative transitional test cases are studied with ILES using the EE and NSE: the TGV at $Re = 3000$ and initial $Ma = 0.28$, and the air-SF₆-air gas curtain subjected to two shock waves at $Ma = 1.2$ studied by Balakumar *et al.* [37]. Grid refinement studies are performed to assess the influence of numerical diffusion on the computations. The simulations are compared against available reference data, and their computational cost analyzed. The paper evaluates the effect of the molecular viscosity and diffusivity on the turbulence and coherent fields, as well as on the mechanisms contributing to the production and diffusion of vorticity.

The results of this paper illustrate the differences between NSE and EE predictions due to viscous effects. In contrast to the EE solutions, the NSE results are in close agreement with the reference data, in particular for the TGV case. On the other hand, the EE solutions lead to meaningful discrepancies with the reference data and only exhibit similarities with the NSE

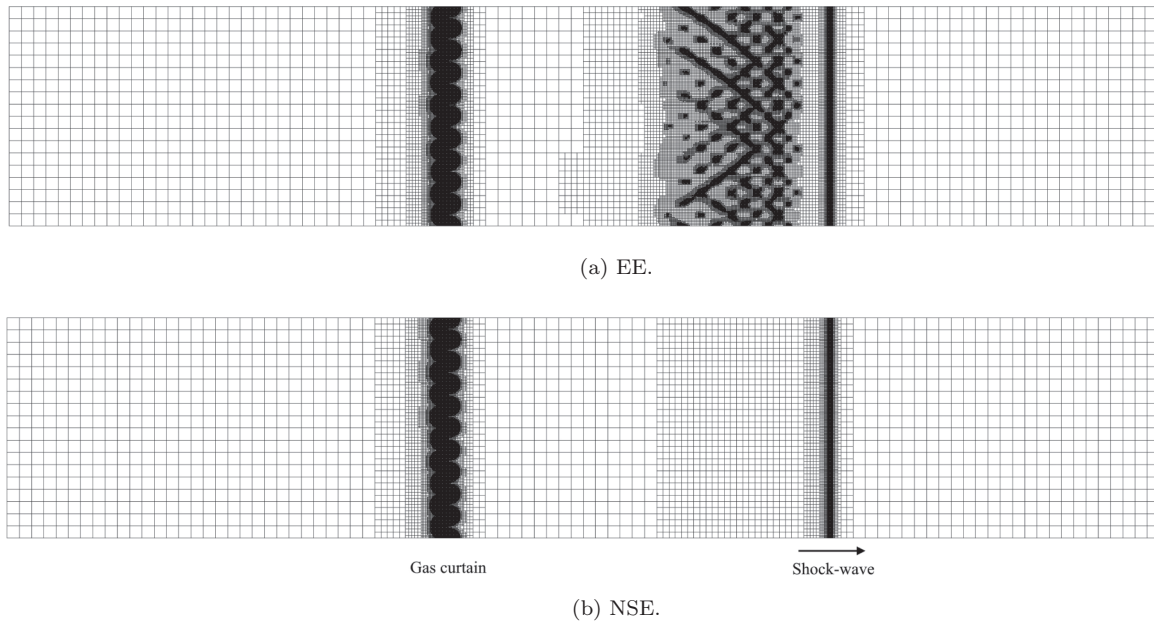


FIG. 25. Spatial resolution of grid g_3 at $t = 220 \mu s$ for EE and NSE.

results at coarse grid resolutions. One of the major contributors to this result is the inability of the EE to bound the Re_c of the computations. The assumption of inviscid flow makes Re_c dependent on the grid resolution so that its magnitude varies upon grid refinement. This aspect is of importance to the prediction of the mean-flow, coherent, and turbulent fields. For instance, it is observed that the turbulence field of inviscid calculations is featured by wider (range of wavelengths) and more energetic inertial ranges than those obtained with the NSE. In regard to the vorticity field, the results show that the EE alter the dynamics of all mechanisms responsible for the production of vorticity. Most notably, the data illustrate that the magnitude of the viscous diffusion of vorticity can even exceed that of the production mechanisms. Finally, it is shown that the cost of performing EE and NSE calculations without AMR is similar. Yet, the utilization of AMR makes the EE significantly more costly than the NSE. In this case, inviscid calculations are at least 2.1 times more expensive than NSE computations. This stems from the larger effective Re achieved by EE simulations, as well as from the inability of this mathematical model to rapidly dissipate fluctuations caused by shock waves.

In summary, this paper demonstrated the importance of molecular viscosity and diffusivity effects on the prediction of transitional and shock-driven mixing flow problems. Our main focus has been on assessing viscous effects; assessing molecular diffusivity effects on scalar predictions deserves

further study and has not been part of the current scope. Naturally, there are applications at full scale involving onset and decay of turbulence where available computational algorithms and resources may be insufficient to reduce the magnitude of numerical diffusion to optimal levels allowing for accurately resolved effects. In these cases, EE and NSE may lead to similar predictions. However, future advances in computing power and the present analysis (cost and accuracy) suggest that the performance of NSE computations may still be advantageous in such cases.

ACKNOWLEDGMENTS

The authors would like to thank K. Prestridge and C. Tomkins for sharing their experimental results. We also thank A. Gowardhan for providing the initial flow conditions of the gas curtain simulations, as well as J. Charonko, S. Jones, and R. Ristorcelli for insightful discussions. Finally, we thank the reviewers for their insightful comments, which led to significant improvements in our paper. Los Alamos National Laboratory (LANL) is operated by TRIAD National Security, LLC for the U.S. Department of Energy (DOE) NNSA. This research was funded by the LANL Mix and Burn project under the DOE ASC, Physics and Engineering Models program. We express our gratitude to the ASC program and the High-Performance Computing division for their dedicated and continued support of this work.

- [1] F. A. Williams, *Combustion Theory: The Fundamental Theory of Chemically Reacting Flow Systems*, 1st ed. (Addison-Wesley, Reading, MA, 1965).
- [2] A. W. Cook, Enthalpy diffusion in multi-component flows, *Phys. Fluids* **21**, 055109 (2009).

- [3] F. F. Grinstein, L. G. Margolin, and W. J. Rider, *Implicit Large Eddy Simulation: Computing Turbulent Flow Dynamics*, 2nd ed. (Cambridge University, New York, 2010).
- [4] C. A. Meakin and D. Arnett, Turbulent convection in stellar interiors. I. Hydrodynamic simulation, *Astrophys. J.* **667**, 448 (2007).

- [5] I. R. Seitzzahl, F. Ciaraldi-Schoolmann, F. K. Röpke, M. Fink, W. Hillebrandt, M. Kromer, R. Pakmor, A. J. Ruitter, S. A. Sim, and S. Taubenberger, Three-dimensional delayed-detonation models with nucleosynthesis for type Ia supernovae, *Mon. Not. R. Astron. Soc.* **429**, 1156 (2013).
- [6] S. W. Bruenn, E. J. Lentz, W. R. Hix, A. Mezzacappa, J. A. Harris, O. E. B. Messer, E. Endeve, J. M. Blondin, M. A. Chertkow, E. J. Lingerfelt, P. Marronetti, and K. N. Yakunin, The development of explosions in axisymmetric Ab initio core-collapse supernova simulations of 12–25 M stars, *Astrophys. J.* **818**, 123 (2016).
- [7] R. L. Holmes, G. Dimonte, B. Fryxell, M. L. Gittings, J. W. Grove, M. Schneider, D. H. Sharp, A. L. Velikovich, R. P. Weaver, and Q. Zhang, Richtmyer-meshkov instability growth: Experiment, simulation and theory, *J. Fluid Mech.* **389**, 55 (1999).
- [8] D. J. Hill, C. Pantano, and D. I. Pullin, Large-eddy simulation and multiscale modelling of a richtmyer-meshkov instability with reshock, *J. Fluid Mech.* **557**, 29 (2006).
- [9] B. Thornber, D. Drikakis, D. L. Youngs, and R. J. R. Williams, The influence of initial conditions on turbulent mixing due to richtmyer-meshkov instability, *J. Fluid Mech.* **654**, 99 (2010).
- [10] J. Yao and D. S. Stewart, On the dynamics of multi-dimensional detonation, *J. Fluid Mech.* **309**, 225 (1996).
- [11] R. Saurel, G. Huber, G. Jourdan, E. Lapébie, and L. Munier, Modelling spherical explosions with turbulent mixing and post-detonation, *Phys. Fluids* **24**, 115101 (2012).
- [12] M. Short and J. J. Quirk, High explosive detonation-confiner interactions, *Annu. Rev. Fluid Mech.* **50**, 215 (2018).
- [13] F. E. Marble, G. J. Hendricks, and E. E. Zukoski, Progress toward shock enhancement of supersonic combustion processes, in *23rd American Institute of Aeronautics and Astronautics (AIAA) Joint Propulsion Conference (AIAA, San Diego, 1987)*, AIAA Paper No. 87-1880, pp. 123–129.
- [14] R. Dubeout, J. P. Sislian, and R. Oppitz, Numerical simulation of hypersonic shock-induced combustion ramjets, *J. Propul. Power* **14**, 869 (1998).
- [15] V. Ahuja, R. J. Hartfield, and A. Shelton, Optimization of hypersonic aircraft using genetic algorithms, *Appl. Math. Comput.* **242**, 423 (2014).
- [16] P. L. Roe, Characteristic-based schemes for the euler equations, *Annu. Rev. Fluid Mech.* **18**, 337 (1986).
- [17] C. Hirsch, *Numerical Computation of Internal and External Flows, Vol. 1: Fundamentals of Numerical Discretization* (Wiley, New York, 1998).
- [18] C. Hirsch, *Numerical Computation of Internal and External Flows, Vol. 2: Computational Methods for Inviscid and Viscous Flows* (Wiley, New York, 1998).
- [19] R. B. Bird, W. E. Stewart, and E. N. Lightfoot, *Transport Phenomena*, 2nd ed. (Wiley, New York, 2002).
- [20] E. F. Toro, *Riemann Solvers and Numerical Methods for Fluid Dynamics*, 3rd ed. (Springer-Verlag, Berlin, 2009).
- [21] F. S. Pereira, L. Eça, and G. Vaz, Verification and validation exercises for the flow around the KVLCC2 tanker at model and full-scale reynolds numbers, *Ocean Engineering* **129**, 133 (2017).
- [22] F. S. Pereira, L. Eça, G. Vaz, and S. S. Girimaji, Challenges in scale-resolving simulations of turbulent wake flows with coherent structures, *J. Comput. Phys.* **363**, 98 (2018).
- [23] F. S. Pereira, L. Eça, G. Vaz, and M. Kerkvliet, Application of second-moment closure to statistically steady flows of practical interest, *Ocean Engineering* **189**, 106372 (2019).
- [24] F. S. Pereira, F. F. Grinstein, and D. Isreal, Effect of the numerical discretization scheme in shock-driven turbulent mixing simulations, *Comput. Fluids* **201**, 104487 (2020).
- [25] V. M. Canuto and J. Christensen-Dalsgaard, Turbulence in astrophysics: Stars, *Annu. Rev. Fluid Mech.* **30**, 167 (1998).
- [26] D. H. Porter and P. R. Woodward, Simulating compressible turbulent flow with PPM, in *Implicit Large Eddy Simulation*, 1st ed. (Cambridge University, Cambridge, England, 2007), Chap. 7, pp. 245–264.
- [27] P. E. Dimotakis, The mixing transition in turbulent flows, *J. Fluid Mech.* **409**, 69 (2000).
- [28] Y. Zhou, Unification and extension of the similarity scaling criteria and mixing transition for studying astrophysics using high energy density laboratory experiments or numerical simulations, *Phys. Plasmas* **14**, 082701 (2007).
- [29] W. George and L. Davidson, Role of initial conditions in establishing asymptotic flow behavior, *AIAA J.* **42**, 438 (2004).
- [30] J. R. Ristorcelli, A. A. Gowardhan, and F. F. Grinstein, Two classes of richtmyer-meshkov instabilities: A detailed statistical look, *Phys. Fluids* **25**, 044106 (2013).
- [31] F. Grinstein, Initial conditions and modeling for simulations of shock driven turbulent material mixing, *Comput. Fluids* **151**, 58 (2017).
- [32] K. O. Mikaelian, Effect of viscosity on rayleigh-taylor and richtmyer-meshkov instabilities, *Phys. Rev. E* **47**, 375 (1993).
- [33] C. R. Weber, D. S. Clark, A. W. Cook, L. E. Busby, and H. F. Robey, Inhibition of turbulence in inertial-confinement-fusion hot spots by viscous dissipation, *Phys. Rev. E* **89**, 053106 (2014).
- [34] J. P. Boris, F. F. Grinstein, E. S. Oran, and R. L. Kolbe, New insights into large eddy simulation, *Fluid Dynamics Research* **10**, 199 (1992).
- [35] G. I. Taylor and A. E. Green, Mechanism of the production of small eddies from large ones, *Proc. R. Soc. A* **158**, 499 (1937).
- [36] M. E. Brachet, D. I. Meiron, S. A. Orzag, B. G. Nickel, R. H. Morf, and U. Frisch, Small scale structure of the taylor-green vortex, *J. Fluid Mech.* **130**, 411 (1983).
- [37] B. J. Balakumar, G. C. Orlicz, C. D. Tomkins, and K. P. Prestridge, Simultaneous particle-image velocimetry-planar laser-induced fluorescence measurements of richtmyer-meshkov instability growth in a gas curtain with and without reshock, *Phys. Fluids* **20**, 124103 (2008).
- [38] D. Drikakis, C. Fureby, F. F. Grinstein, and D. Youngs, Simulation of transition and turbulence decay in the taylor-green vortex, *J. Turbulence* **8**, N20 (2007).
- [39] M. Gittings, R. Weaver, M. Clover, T. Betlach, N. Byrne, R. Coker, E. Dendy, R. Hueckstaedt, K. New, W. R. Oakes, D. Ranta, and R. Stefan, The RAGE radiation-hydrodynamic code, *Comput. Sci. Discovery* **1**, 015005 (2008).
- [40] S. Kida and M. Takaoka, Vortex reconnection, *Annu. Rev. Fluid Dyn.* **26**, 169 (1994).
- [41] Y. Yang and D. I. Pullin, Evolution of vortex-surface fields in viscous taylor-green and kida-pelz flows, *J. Fluid Mech.* **685**, 146 (2011).
- [42] J. B. Bell and D. L. Marcus, Vorticity intensification and transition to turbulence in three-dimensional euler equations, *Commun. Math. Phys.* **147**, 371 (1992).

- [43] S. Tanveer and C. G. Speziale, Singularities of the euler equation and hydrodynamic stability, *Phys. Fluids A: Fluid Dyn.* **5**, 1456 (1993).
- [44] J. D. Gibbon and M. Heritage, Angular dependence and growth of vorticity in the three-dimensional euler equations, *Phys. Fluids* **9**, 901 (1997).
- [45] E. Behr, J. Nečas, and H. Wu, On blow-up of solution for euler equations, *Math. Modell. Numer. Anal.* **35**, 229 (2001).
- [46] U. Frisch, T. Matsumoto, and J. Bec, Singularities of euler flow? not out of the blue!, *J. Stat. Phys.* **113**, 761 (2006).
- [47] M. P. Brenner, S. Hormoz, and A. Pumir, Potential singularity mechanism for the euler equations, *Phys. Rev. Fluids* **1**, 084503 (2016).
- [48] F. F. Grinstein, Self-induced vortex ring dynamics in subsonic rectangular jets, *Phys. Fluids* **7**, 2519 (1995).
- [49] F. F. Grinstein, Vortex dynamics and entrainment in rectangular free jets, *J. Fluid Mech.* **437**, 69 (2001).
- [50] C. Fureby and F. F. Grinstein, Large eddy simulation of high-reynolds-number free and wall-bounded flow, *J. Comput. Phys.* **181**, 68 (2002).
- [51] F. F. Grinstein, Coarse grained simulation of convectively driven turbulent mixing, transition, and turbulence decay, *Physica D* **407**, 132419 (2020).
- [52] M. Lesieur and S. Ossia, 3D isotropic turbulence at very high reynolds numbers: EDQNM study, *J. Turbulence* **1**, N7 (2000).
- [53] F. F. Grinstein, A. A. Gowardhan, and A. J. Wachtor, Simulations of richtmyer-meshkov instabilities in planar shock-tube experiments, *Phys. Fluids* **23**, 034106 (2011).
- [54] A. A. Gowardhan and F. F. Grinstein, Numerical simulation of richtmyer-meshkov instabilities in shocked gas curtains, *J. Turbulence* **12**, 1 (2011).
- [55] R. D. Richtmyer, Taylor instability in shock acceleration of compressible fluids, *Commun. Pure Appl. Math.* **13**, 297 (1960).
- [56] E. E. Meshkov, Instability of the interface of two gases accelerated by a shock wave, *Fluid Dyn.* **4**, 101 (1969).
- [57] L. Rayleigh, Investigation of the character of the equilibrium of an incompressible heavy fluid of variable density, *Proc. London Math. Soc.* **s1-14**, 170 (1882).
- [58] G. Taylor, The instability of liquid surfaces when accelerated in a direction perpendicular to their planes, *Proc. R. Soc. A* **201**, 192 (1950).
- [59] W. Thomson, Hydrokinetic solutions and observation, *London, Edinburgh Dublin Philos. Mag. J. Sci.* **42**, 362 (1871).
- [60] H. von Helmholtz, On discontinuous movements of fluids, *London, Edinburgh Dublin Philos. Mag. J. Sci.* **36**, 337 (1868).
- [61] M. Brouillette, The richtmyer-meshkov instability, *Annu. Rev. Fluid Mech.* **34**, 445 (2002).
- [62] Y. Zhou, Rayleigh-taylor and richtmyer-meshkov instability induced flow, turbulence, and mixing. I, *Phys. Rep.* **720–722**, 1 (2017).
- [63] Y. Zhou, Rayleigh-taylor and richtmyer-meshkov instability induced flow, turbulence, and mixing. II, *Phys. Rep.* **723–725**, 1 (2017).
- [64] J. J. Charonko and K. Prestridge, Variable-density mixing in turbulent jets with coflow, *J. Fluid Mech.* **825**, 887 (2019).
- [65] http://www.engineeringtoolbox.com/air-diffusion-coefficient-gas-mixture-temperature-d_2010.html (2019).
- [66] E. F. Toro, M. Spruce, and W. Speares, Restoration of the contact surface in the hll-riemann solver, *Shock Waves* **4**, 25 (1994).
- [67] P. Colella and P. R. Woodward, The piecewise parabolic method (ppm) for gas-dynamical simulations, *J. Comput. Phys.* **54**, 174 (1984).
- [68] B. Thornber, A. Mosedale, D. Drikakis, D. Youngs, and R. J. R. Williams, An improved reconstruction method for compressible flows with low mach number features, *J. Comput. Phys.* **227**, 4873 (2008).
- [69] B. van Leer, Towards the ultimate conservative difference scheme, *J. Comput. Phys.* **135**, 229 (1997).
- [70] B. M. Haines, F. F. Grinstein, and J. R. Fincke, Three-dimensional simulation strategy to determine the effects of turbulent mixing on inertial-confinement-fusion capsule performance, *Phys. Rev. E* **89**, 053302 (2014).
- [71] B. M. Haines, E. L. Vold, K. Molvig, C. Aldrich, and R. Rauenzahn, The effects of plasma diffusion and viscosity on turbulent instability growth, *Phys. Plasmas* **21**, 092306 (2014).
- [72] K. Molvig, A. N. Simakov, and E. L. Vold, Classical transport equations for burning gas-metal plasmas, *Phys. Plasmas* **21**, 092709 (2014).
- [73] E. L. Vold, R. M. Rauenzahn, C. H. Aldrich, K. Molvig, A. N. Simakov, and B. M. Haines, Plasma transport in an eulerian amr code, *Plasma Phys.* **24**, 042702 (2017).
- [74] W. Kokkinakis, D. Drikakis, D. L. Youngs, and R. J. R. Williams, Two-equation and multi-fluid turbulence models for rayleigh-taylor mixing, *Int. J. Heat Fluid Flow* **56**, 233 (2015).
- [75] A. J. A. Favre, Equations statistiques des gaz turbulents, *C. R. Acad. Sci.* **246**, 2576 (1958); **246**, 2723 (1958); **246**, 2839 (1958); **246**, 3216 (1958).
- [76] A. Favre, Équations statistiques aux fluctuations d'Entropie, de concentration, de rotationnel dans les écoulements compressibles, *C. R. Acad. Sci.* **273**, 1289 (1971).
- [77] A. Favre, Équations statistiques des gaz turbulents compressibles. I. formes générales, *J. Mec.* **4**, 361 (1965).
- [78] A. Favre, Équations statistiques des gaz turbulents compressibles. II. méthode des vitesses moyennes; méthode des vitesses macroscopiques pondérées par la masse volumique, *J. Mec.* **4**, 391 (1965).
- [79] C.-W. Shu, W.-S. Don, D. Gottlieb, O. Schilling, and L. Jameson, Numerical convergence study of nearly incompressible, inviscid taylor-green vortex flow, *J. Sci. Comput.* **24**, 1 (2005).
- [80] R. H. Morf, S. A. Orszag, and U. Frisch, Spontaneous Singularity in Three-Dimensional Inviscid, Incompressible Flow, *Phys. Rev. Lett.* **44**, 572 (1980).
- [81] The American Society of Mechanical Engineers (ASME), *Standard for Verification and Validation in Computational Fluid Dynamics and Heat Transfer: ASME V&V 20-2009* (ASME, New York, 2009).
- [82] L. Eça and M. Hoekstra, A procedure for the estimation of the numerical uncertainty of cfd calculations based on grid refinement studies, *J. Comput. Phys.* **262**, 104 (2014).
- [83] J. Jeong and F. Hussain, On the identification of a vortex, *J. Fluid Mech.* **285**, 69 (1995).
- [84] F. S. Pereira, F. F. Grinstein, D. Israel, and R. Rauenzahn, Modeling and simulation of transitional taylor-green vortex flow with PANS (unpublished).

- [85] M. E. Brachet, Direct simulation of three-dimensional turbulence in the Taylor-Green vortex, *Fluid Dynamics Research* **8**, 1 (1991).
- [86] D. Besnard, F. H. Harlow, R. M. Rauenzahn, and C. Zemach, Turbulence transport equations for variable-density turbulence and their relationship to two-field models, Technical Reports No. LA-12303-MS and No. DE92 017292, Los Alamos National Laboratory, 1992 (unpublished).
- [87] K. Stalsberg-Zarling and R. Gore, The BHR2 turbulence model: Incompressible isotropic decay, Rayleigh-Taylor, Kelvin-Helmholtz and homogeneous variable density turbulence, Technical Report No. LA-UR-11-04773, Los Alamos National Laboratory, 2011 (unpublished).
- [88] D. C. Wilcox, *Turbulence Modeling for CFD*, 3rd ed. (DCW, La Cañada, 2006).
- [89] Y. Zhou, F. F. Grinstein, A. J. Wachtor, and B. M. Haines, Estimating the effective Reynolds number in implicit large-eddy simulation, *Phys. Rev. E* **89**, 013303 (2014).
- [90] H. Tennekes and J. L. Lumley, *A First Course in Turbulence* (MIT, Cambridge, MA, 1972).
- [91] P. A. Davidson, *Turbulence: An Introduction for Scientists and Engineers* (Oxford University, London, 2006).
- [92] P. Chassaing, R. A. Antonia, F. Anselmetti, L. Joly, and S. Sarkar, *Variable Density Fluid Turbulence*, Fluid Mechanics and Its Applications, Vol. 69 (Springer, New York, 2002).
- [93] T. Gatski and J.-P. Bonnet, *Compressibility, Turbulence and High Speed Flow*, 1st ed. (Elsevier, Amsterdam, 2009).
- [94] N. J. Nelson and F. F. Grinstein, Effects of initial condition spectral content on shock-driven turbulent mixing, *Phys. Rev. E* **92**, 013014 (2015).
- [95] F. F. Grinstein, J. A. Saenz, J. C. Dolence, T. O. Masser, R. M. Rauenzahn, and M. M. Francois, Effects of operator splitting and low Mach-number correction in turbulent mixing transition simulations, *Comput. Math. Appl.* **78**, 437 (2019).
- [96] A. Hussain and W. Reynolds, The mechanics of an organized wave in turbulent shear flow, *J. Fluid Mech.* **41**, 241 (1970).
- [97] R. Schiestel, Multiple-time-scale modeling of turbulent flows in one-point closures, *Phys. Fluids* **30**, 722 (1987).